Comparison of airborne measurements of NO, NO$_2$, HONO, NO$_y$ and CO during FIREX-AQ

Ilann Bourgeois[1,2], Jeff Peischl[1,2], J. Andrew Neuman[1,2], Steven S. Brown[2,3], Hannah M. Allen[4], Pedro Campuzano-Jost[1,3], Matthew M. Coggon[1,2], Joshua P. DiGangi[5], Glenn S. Diskin[5], Jessica B. Gilman[2], Georgios I. Gkatzelis[1,2,a], Hongyu Guo[1,3], Hannah A. Halliday[5,b], Thomas F. Hanisco[6], Christopher D. Holmes[7], L. Gregory Huey[8], Jose L. Jimenez[1,3], Aaron D. Lamplugh[1,2], Young Ro Lee[8], Jakob Lindaas[9], Richard H. Moore[5], John B. Nowak[5], Demetrios Pagonis[1,3,c], Pamela S. Rickly[1,2], Michael A. Robinson[1,2,3], Andrew W. Rollins[2], Vanessa Selimovic[10], Jason M. St. Clair[6,11], David Tanner[8], Krystal T. Vasquez[4], Patrick R. Veres[2], Carsten Warneke[2], Paul O. Wennberg[12,13], Rebecca A. Washenfelder[2], Elizabeth B. Wiggins[5], Caroline C. Womack[1,2], Lu Xu[12,d], Kyle J. Zarzana[1,2,e] and Thomas B. Ryerson[2,f]

[1]Cooperative Institute for Research in Environmental Sciences, University of Colorado Boulder, Boulder, CO, USA
[2]NOAA Chemical Sciences Laboratory (CSL), Boulder, CO, USA
[3]Department of Chemistry, University of Colorado Boulder, Boulder, CO, USA
[4]Division of Chemistry and Chemical Engineering, California Institute of Technology, Pasadena, CA, USA
[5]NASA Langley Research Center, Hampton, VA, USA
[6]Atmospheric Chemistry and Dynamics Laboratory, NASA Goddard Space Flight Center, Greenbelt, MD, USA
[7]Department of Earth, Ocean and Atmospheric Science, Florida State University, Tallahassee, FL, USA
[8]School of Earth and Atmospheric Sciences, Georgia Institute of Technology, Atlanta, GA, USA
[9]Department of Atmospheric Science, Colorado State University, Fort Collins, CO, USA
[10]Department of Chemistry and Biochemistry, University of Montana, Missoula, MT, USA
[11]Joint Center for Earth Systems Technology, University of Maryland Baltimore County, Baltimore, MD, USA
[12]Division of Geological and Planetary Sciences, California Institute of Technology, Pasadena, CA, USA
[13]Division of Engineering and Applied Science, California Institute of Technology, Pasadena, CA, USA

[a]now at Institute of Energy and Climate Research, IEK-8: Troposphere, Forschungszentrum Jülich GmbH, Jülich, Germany
[b]now at Office of Research and Development, US EPA, Research Triangle Park, NC, USA
[c]now at Department of Chemistry and Biochemistry, Weber State University, Ogden, UT, USA
[d]now at 1 and 2
[e]now at 3
[f]now at Scientific Aviation, Boulder, CO, USA

Abstract

1   We present a comparison of fast-response instruments installed onboard the NASA DC-8
2   aircraft that measured nitrogen oxides (NO and NO_2), nitrous acid (HONO), total reactive
3   odd nitrogen (measured both as the total (NO_y) and from the sum of individually measured
4   species (ΣNO_y)) and carbon monoxide (CO) in the troposphere during the 2019 Fire
5   Influence on Regional to Global Environments and Air Quality (FIREX-AQ) campaign. By
6   targeting smoke from summertime wildfires, prescribed fires and agricultural burns across
7   the continental United States, FIREX-AQ provided a unique opportunity to investigate
8   measurement accuracy in concentrated plumes where hundreds of species coexist. Here, we
9   compare NO measurements by chemiluminescence (CL) and laser induced fluorescence
10 (LIF); NO_2 measurements by CL, LIF and cavity enhanced spectroscopy (CES); HONO
11 measurements by CES and iodide-adduct chemical ionization mass spectrometry (CIMS);
12 and CO measurements by tunable diode laser absorption spectrometry (TDLAS) and
13 integrated cavity output spectroscopy (ICOS). Additionally, total NO_y measurements using
14 the CL instrument were compared with ΣNO_y (= NO + NO_2 + HONO + nitric acid (HNO_3) +
15 acyl peroxy nitrates (APNs) + submicron particulate nitrate (pNO_3)). Other NO_y species were
16 not included in ΣNO_y as they either contributed minimally to it (e.g., C_1–C_5 alkyl nitrates,
17 nitryl chloride ($ClNO_2$), dinitrogen pentoxide (N_2O_5)) or were not measured during FIREX-
18 AQ (e.g., higher oxidized alkyl nitrates, nitrate (NO_3), non-acyl peroxynitrates, coarse mode
19 aerosol nitrate). The aircraft instrument intercomparisons demonstrate the following: 1) NO
20 measurements by CL and LIF agreed well within instrument uncertainties, but with
21 potentially reduced time response for the CL instrument; 2) NO_2 measurements by LIF and
22 CES agreed well within instrument uncertainties, but CL NO_2 was on average 10% higher; 3)
23 CES and CIMS HONO measurements were highly correlated in each fire plume transect, but
24 the correlation slope of CES vs. CIMS for all 1 Hz data during FIREX-AQ was 1.8, which
25 we attribute to a reduction in the CIMS sensitivity to HONO in high temperature
26 environments; 4) NO_y budget closure was demonstrated for all flights within the combined
27 instrument uncertainties of 25%. However, we used a fluid dynamic flow model to estimate
28 that average pNO_3 sampling fraction through the NO_y inlet in smoke was variable from one
29 flight to another and ranged between 0.36 and 0.99, meaning that approximately 0–24% on
30 average of the total measured NO_y in smoke may have been unaccounted for and may be due
31 to unmeasured species such as organic nitrates; 5) CO measurements by ICOS and TDLAS
32 agreed well within combined instrument uncertainties, but with a systematic offset that
33 averaged 2.87 ppbv; and 6) integrating smoke plumes followed by fitting the integrated
34 values of each plume improved the correlation between independent measurements.

1. Introduction

Biomass burning (BB) can take multiple forms (e.g., wildfires, prescribed fires, agricultural burns, grass fires, peat fires) and accounts for a large fraction of global carbon emissions with consequences for climate (Bowman et al., 2009; van der Werf et al., 2010, 2017) and biogeochemical cycles (Crutzen & Andreae, 2016). BB also contributes substantially to the atmospheric burden of trace gases and aerosols (Andreae, 2019), causing poor air quality on regional to continental scales (Jaffe et al., 2020; O'Dell et al., 2019; Wotawa, 2000) and posing a major threat to public health (Johnston et al., 2012, 2021). In the United States (US), wildfires mainly occur in the western states and in Alaska and burned over 4.5 million acres in 2019 (US National Interagency Fire Center, https://www.nifc.gov/fire-information). Wildfires frequency and severity are predicted to increase in response to a warmer, drier climate (Burke et al., 2021; Westerling, 2016) and also to increasing human-caused ignition (Balch et al., 2017). In comparison, prescribed fires, which are common practice in the southeastern US, burned an estimated 10 million acres in 2019, to which agricultural burns added another 2–3 million acres (Melvin, 2020). While agricultural burns are usually smaller and less intense than wildfires or prescribed fires, they occur more frequently and throughout the whole year, and can significantly impact local air quality (Dennis et al., 2002; McCarty, 2011).

Rising interest in the impact of fires on climate and air quality over the past decades has resulted in a series of laboratory studies of BB emissions in the US such as the FLAME-4 experiment in 2012 (e.g., Stockwell et al., 2014) and the FIRELAB study in 2016 (e.g., Selimovic et al., 2018). Recent, large-scale field studies such as AMMA (e.g., Liousse et al., 2010), BBOP (e.g., Collier et al., 2016) and WE-CAN (e.g., Juncosa Calahorrano et al. (2021)) have been dedicated to sampling and characterizing emissions and atmospheric chemistry from fires. The focus of the joint National Oceanic and Atmospheric Administration (NOAA) / National Aeronautics and Space Administration (NASA) Fire Influence on Regional to Global Environments and Air Quality (FIREX-AQ) airborne campaign was to provide comprehensive observations to investigate the impact of summer time wildfires, prescribed fires and agricultural burns on air quality and climate across the conterminous US (Warneke et al., 2022).

Accurate measurements facilitate understanding of fire emissions, processing and impacts. In situ, fast-response measurements of trace gases in the atmosphere conducted from airborne platforms provide unique data sets that enhance our understanding of atmospheric composition and chemistry. One method for evaluating measurement accuracy is by comparison of independent measurements using different techniques. A relatively small body of literature reported comparisons of methods for in flight detection of tropospheric carbon monoxide (CO) and reactive odd nitrogen species measured both as the total (NO_y) and from the sum of individually measured species (ΣNO_y), and these studies have shown that such comparisons are valuable for identifying instrument artifacts and quantifying measurement uncertainties (Eisele et al., 2003; Gregory et al., 1990; Hoell et al., 1987; Hoell et al., 1987; Sparks et al., 2019). During FIREX-AQ, a large suite of airborne instruments, detailed in the following sections, performed independent in situ tropospheric measurements of one or more fire-science relevant reactive nitrogen species and CO aboard the NASA DC-8 aircraft (Table

79   1). Additionally, FIREX-AQ provides a unique opportunity to investigate measurement
80   accuracy in concentrated smoke plumes where hundreds of species coexist.
81
82   Nitric oxide (NO) and nitrogen dioxide (NO_2) are among the largest components of the
83   reactive nitrogen budget emitted by biomass burning and are produced by the oxidation of
84   reduced nitrogen species present in the fuel in the flaming stage of combustion (Roberts et
85   al., 2020). NO_x, defined as the sum of NO and NO_2, directly affects atmospheric oxidation
86   rates and ozone (O_3) production within fire plumes (Robinson et al., 2021; Xu et al., 2021). It
87   also contributes to the formation of secondary aerosols and N transport and deposition to
88   ecosystems downwind (Galloway et al., 2003; Kroll & Seinfeld, 2008; Ziemann & Atkinson,
89   2012). Therefore, two independent NO and three independent NO_2 measurements were part
90   of FIREX-AQ to provide continuous in situ observations, as described in section 2 below.
91   Nitrous acid (HONO) is emitted directly to the atmosphere through various combustion
92   processes including BB. The rapid production of OH from HONO at the early stage of smoke
93   plume formation (Peng et al., 2020) results in rapid initiation of photochemistry, with a
94   strong influence on downwind chemical evolution of smoke plumes (Bourgeois et al., 2021;
95   Robinson et al., 2021; Theys et al., 2020). Total NO_y can be measured through conversion of
96   individual species to NO (Fahey et al., 1985). It is a more conserved tracer for NO_x emissions
97   than NO_x itself since it accounts for NO_x oxidation products, and it provides a mean to assess
98   from a mass-balance approach the accuracy of ΣNO_y budget closure (Bollinger et al., 1983;
99   Fahey et al., 1986; Williams et al., 1997). Fahey et al. (1986) define ΣNO_y as the sum of
100   important nitrogen species as illustrated by Eq. 1:
101
102   ΣNO_y = NO + NO_2 + nitric acid (HNO_3) + HONO + peroxynitric acid (HO_2NO_2) + nitrate
103   (NO_3) + dinitrogen pentoxide ($2 \times N_2O_5$) + peroxyacetyl nitrate (PAN) + particulate nitrate
104   (pNO_3) + …   (Eq. 1)
105
106   Other nitrogen compounds that can contribute to ΣNO_y include alkyl nitrates (Day et al.,
107   2003), acyl peroxynitrates (APNs; Juncosa Calahorrano et al., 2021), non-acyl peroxynitrates
108   (RO_2NO_2 ; Murphy et al., 2004), nitryl chloride ($ClNO_2$; Kenagy et al., 2018), nitro
109   compounds and nitroaromatics (Decker et al., 2021).
110
111   Carbon monoxide (CO) is emitted from incomplete combustion in fires and other sources,
112   and is especially important for characterizing the combustion stage of fires (i.e., flaming vs.
113   smoldering) through the use of the modified combustion efficiency (Yokelson et al., 1996).
114   Due to its relatively long chemical lifetime, CO is commonly used as a conserved tracer to
115   account for dilution with ambient air as smoke plumes are transported downwind, and
116   accurate CO measurements are necessary to better constrain emission factors (EFs) used in
117   emission inventories.
118
119   This study builds on past airborne instrument comparisons and extends these analyses to a
120   new species (HONO), new measurement techniques (first airborne deployment of the NOAA
121   NO-LIF (laser induced fluorescence) and the NOAA CO-ICOS (integrated cavity output
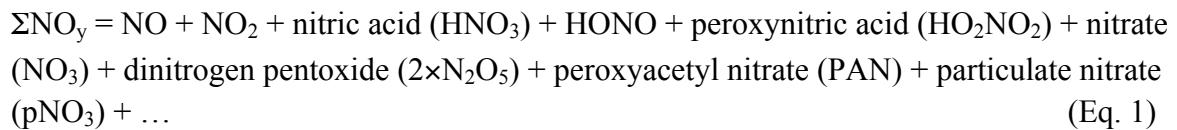
122 spectroscopy) instruments) and new environments (concentrated fire smoke). In this paper we
123 present a comparison of NO, NO_2, HONO, NO_y and CO measurements, which are
124 compounds of major interest for fire-related science, air quality and climate. In the first part
125 of this paper, we describe the FIREX-AQ campaign, the deployed instruments and the
126 methodology used to perform the comparisons. In the second part, we provide a detailed
127 instrument comparison for each species.
128
129 **2. FIREX-AQ overview and instruments**
130   2.1 <u>FIREX-AQ airborne mission</u>
131 The FIREX-AQ campaign (https://www-air.larc.nasa.gov/missions/firex-aq/;
132 https://www.esrl.noaa.gov/csl/projects/firex-aq/) took place from July to September 2019.
133 FIREX-AQ included the deployment of multiple aircraft and mobile platforms over the
134 course of the campaign, however this study focuses on the heavily instrumented NASA DC-8
135 aircraft. The NASA DC-8 portion of the project achieved two flights over the Los Angeles
136 (LA) Basin and the Central Valley in California, 13 flights originating from Boise, Idaho, and
137 7 flights based out of Salina, Kansas. The flights from Boise were conducted over the
138 Western US to sample smoke from wildfires, while the flights from Salina focused on
139 agricultural and prescribed burns (hereafter referred to as eastern fires) in the Southeastern
140 US.
141
142 Most wildfire flights were designed to sample background mixing ratios, fresh emissions, and
143 aged smoke, whereas the eastern fire flights typically transected numerous fresh smoke
144 plumes several times each. For wildfires, the NASA DC-8 first flew upwind of the fire to
145 characterize ambient conditions unaffected by targeted fire emissions. Subsequent cross-wind
146 plume transects were conducted as close as possible to the fire to sample the emissions with
147 the least possible atmospheric ageing. Plume transects were designed to be perpendicular to
148 the wind direction and through the center of the vertical extent of the plume, terrain
149 permitting. The vertical structure of the plume was systematically assessed using a
150 differential absorption lidar during a lengthwise overpass above the plume from end to start.
151 The aircraft transected the smoke plume successively further downwind, at approximately
152 15–40 km intervals, to characterize smoke evolution in a "lawnmower" pattern (Figure 1a).
153 For several wildfires, the DC-8 also executed flight transects along the plume axis, both
154 toward and away from the fire source. Most eastern fires sampled during FIREX-AQ did not
155 produce plumes large enough to enable regularly spaced plume transects. Most smoke plumes
156 were therefore sampled repetitively at the same location, sometimes with varying altitude
157 and/or approach angle (Figure 1b).
158
159   2.2 <u>Instruments</u>
160   2.2.1   Chemiluminescence (NO/NO_2/NO_y)
161 The NOAA CL instrument has been frequently used for both ground-based and airborne
162 measurements of NO, NO_2 and NO_y and uses the CL detection of NO with O_3 added as
163 reagent gas (Fontijn et al., 1970; Ridley & Grahek, 1990; Ridley & Howlett, 1974; Ryerson
164 et al., 1999, 2000). NO, NO_2 and NO_y are measured on three independent channels of the
165 instrument. The NO channel measures NO, the NO_2 channel measures the sum of NO and

166 photolyzed NO_2 as NO, and the NO_y channel measures the total reactive nitrogen oxides
167 species reduced to NO. NO_2 is determined from the difference between signals from the NO
168 and NO_2 channels. Ambient air is continuously sampled from a pressure-building ducted
169 aircraft inlet to the instrument at a typical flow of 1045.1 ± 0.2, 1030.2 ± 0.2 and 1029.5 ±
170 0.2 standard cubic centimeters per minute (sccm) in flight for NO, NO_2, and NO_y,
171 respectively. In the NO_2 channel, NO_2 is photolyzed to NO with a 40 ± 1 % conversion
172 efficiency using two ultraviolet (UV) LEDs (Hamamatsu, model L11921) at 385 nm in a 45
173 cm long quartz cell (inner diameter of 1.2 cm) pressure-controlled at 209.8 ± 0.3 Torr. In the
174 NO channel, a similar quartz cell wrapped in aluminum foil to avoid NO_2 photolysis and
175 pressure controlled at 209.7 ± 0.3 Torr, ensures similar residence time of sampled air in both
176 channels. In the NO_y channel, reactive odd nitrogen species are first sampled through an inlet
177 heated at 90.0 ± 0.1°C then catalytically reduced to NO on a gold tube surface heated at
178 300.0 ± 0.2°C in the presence of added pure CO flowing at 3.19 ± 0.01 sccm. Approximately
179 5% O_3 in oxygen is produced by corona discharge, delivered at 73.80 ± 0.02 (NO channel),
180 74.11 ± 0.03 (NO_2 channel), and 74.60 ± 0.04 (NO_y channel) sccm, and mixed with sampled
181 air in a pressure (8.65 ± 0.02, 8.79 ± 0.02, 8.56 ± 0.02 Torr for NO, NO_2, and NO_y
182 respectively) and temperature (25.0 ± 0.2, 25.1 ± 0.2 and 25.1 ± 0.2°C for NO, NO_2 and NO_y,
183 respectively) controlled reaction vessel. O_3-induced CL is detected with a red-sensitive
184 photomultiplier tube controlled at −78°C with dry ice, and the amplified digitized signal is
185 recorded using an 80 MHz counter. Pulse coincidence at high count rates was calculated after
186 the mission by fitting an inverse function to the curve between observed and theoretical count
187 rates for known NO mixing ratios ranging from ppbv to ppmv levels. Instrument calibrations
188 were routinely performed both on the ground and during flight by standard addition of NO
189 from a gravimetrically determined NO in N_2 mixture (1.38 ± 0.03 ppmv) delivered at 4.04 ±
190 0.02 (NO channel), 4.84 ± 0.02 (NO_2 channel), and 4.96 ± 0.02 (NO_y channel) sccm. All
191 measurements were taken at a temporal resolution of 0.1 second (s), averaged to 1 s, and
192 corrected for the dependence of instrument sensitivity on ambient water vapor content
193 (Ridley et al., 1992). Finally, NO_2 data were further corrected for a HONO interference (5%
194 of the HONO mixing ratios) due to HONO photolysis at 385 nm quantified from theoretical
195 calculation and confirmed in the laboratory using a HONO source described in Lao et al.
196 (2020). Under these conditions the total estimated 1Hz uncertainty at sea level was ± (4 % +
197 6 pptv), ± (7 % + 20 pptv), and ± (12 % + 15 pptv) for NO, NO_2, and NO_y, respectively.
198
199   2.2.2   Laser Induced Florescence (NO)
200 The NOAA NO-LIF measurements were performed using a custom-built laser-induced
201 fluorescence instrument as detailed in Rollins et al. (2020). Air was continuously sampled
202 from outside the aircraft through an optical cell in the DC-8 cabin held to near 90 hPa. The
203 instrument utilizes a fiber laser system with a narrow-band laser tuned to a rotationally
204 resolved NO spectral feature near 215 nm. Rapid dithering on and off of this resonance
205 achieves 0.1 s measurements with a continuously monitored background to reduce
206 uncertainty in the instrument zero. The laser induced excitation of NO is followed by red-
207 shifted fluorescence which is detected by a photomultiplier tube operated in single-photon
208 counting mode. The laser is directed through both a sampling and reference cell in a single
209 pass for continuous monitoring of any changes in the instrument sensitivity due to changes in

the laser spectrum, or pressure of the optical cells. 500 ppbv of NO in air was flown at 50 sccm through the reference cell to ensure that measurements are occurring with the laser tuned to the peak online wavelength. A constant flow of approximately 2500 sccm is maintained within the sampling cell through the use of a custom inlet valve (Gao et al., 1999) and the exhaust of both cells are tied together allowing for any changes in sensitivity due to pressure fluctuations to be accounted for during data reduction. Hourly calibrations were performed during each flight in which 2–10 sccm of 5 ppmv NO in N_2 mixture was added to the sample flow resulting in mixing ratios of 4–20 ppbv. As discussed in Rollins et al (2020), given the sensitivity typically observed during FIREX, nonlinearity associated with saturation of the LIF instrument is not problematic until mixing ratios well above 100 ppbv are encountered. The sensitivity of the instrument was determined using the in-flight calibrations to be typically 10 counts per second (CPS) pptv^{-1} with 10 CPS background achieving a detection limit of 1 pptv for 1 s integration. The uncertainty of the instrument sensitivity is ± 6–9%. The effect of water vapor, which reduces the sensitivity by quenching of the electronically excited NO, was accounted for during data reduction using water vapor measurements provided by an ICOS instrument on the DC-8. The NO measurement uncertainty is estimated to be ± (8% + 1 pptv).

2.2.3   Laser Induced Fluorescence (NO_2)

The NASA Compact Airborne NO_2 Experiment (CANOE) measured NO_2 using non-resonant LIF. The instrument is a modified version of a formaldehyde (HCHO) instrument (St. Clair et al., 2019) with the excitation wavelength changed to 532 nm. The technique utilizes the pulsed (80 kHz) output of a fixed wavelength, 2W, 532 nm laser to excite NO_2 molecules and detects the resulting fluorescence with two identical detection axes consisting of a photomultiplier tube (PMT) and optical filters that transmit > 695 nm. Delayed time gate PMT counts are recorded at 10 Hz and a laboratory calibration, along with an intercept determined by preflight zeroing, are used to provide 1Hz NO_2 data. The NO_2 measurement uncertainty is estimated to be ± (10% + 100 pptv).

During FIREX-AQ, ambient air was sampled using a shared inlet that provided a large (10–25 standard liter per minute (slpm)) bypass flow to the instrument rack. The inlet tube is a 45 cm length of 0.94 cm inner diameter Silcosteel (Restek) coated with FluoroPel (Cazorla et al., 2015). The CANOE instrument pulled its 750 sccm sample flow from a shared manifold (with another four instruments) at the instrument rack. An inline particle filter on the sample line prevented laser scatter by fine aerosol that were not removed by the particle-rejecting inlet. A manual three-way valve outside the instrument was used to sample from a scrubber (Drierite/molecular sieve) and provides a zero before and periodically during the flight. Pressure in the CANOE detection cell was maintained at 40 Torr by a pressure controller that precedes the cell in the flow path.

2.2.4   Cavity Enhanced Spectroscopy (NO_2/HONO)

NO_2 and HONO were also measured by the NOAA airborne cavity enhanced spectroscopy (ACES) instrument. This technique is based on incoherent broadband cavity enhanced

254   spectroscopy (CES, Fiedler et al., 2003). The CES instrument is described in full detail by
255   Min et al. (2016) with only minor changes for FIREX-AQ. Briefly, the system consists of
256   two parallel 45 cm optical cavities capped by highly reflective mirrors, with reflectivity
257   curves centered at 365 nm (R = 0.99987) and 455 nm (R = 0.99992). Each cavity is
258   illuminated by a broadband LED light source (centered at 365 and 455 nm respectively)
259   collimated by an off-axis parabola, and passively coupled into the cavity. The light makes
260   many passes before exiting the cavity into a fiber optic cable, which transmits the light to a
261   grating spectrometer spanning 350–475 nm. The LEDs are modulated on for 0.4 s and off for
262   0.08 s for charged-couple device (CCD) readout, giving a total integration time of 0.48 s per
263   light intensity spectrum. An absorption spectrum of the ambient air sample is determined
264   using the procedure presented by Washenfelder et al. (2008). The procedure requires
265   comparing the measured light intensity spectrum to a background spectrum of the cavity
266   filled with cylinder zero air, which is determined here every 10 minutes. The mirror
267   reflectivity is measured every hour using the Rayleigh scattering difference between helium
268   and zero air, and the spectrometer dark counts and wavelength calibration are measured every
269   two hours. A small flow from a mixture of 25 ppm NO_2 in air is diluted into the cavity every
270   hour, resulting in NO_2 concentrations between 50 and 100 ppbv, to assess the NO_2 spectral
271   retrieval features on the spectrometer. The absolute concentration was not used for calibration
272   of the NO_2 response, but rather for providing a reference NO_2 spectrum. Glyoxal reference
273   spectra was obtained by bubbling zero air through a Teflon bubbler with 40% glyoxal in
274   water as in Min et al. (2016).
275
276   Ambient air is pulled through the inlet into the two optical cavities at a flow rate of 5.4
277   volumetric liters per minute per cavity by a scroll pump. The air passes through two 1 μm
278   pore size Teflon filters (changed before each flight) before entering the instrument to remove
279   any aerosol particles. Mirror cleanliness is maintained by flowing 150 sccm cylinder zero air
280   over each mirror to prevent condensation of semi-volatile species. A pressure controller
281   consisting of a Teflon orifice and a variable flow to a bypass maintains the internal pressure
282   at one of two pressure set points: 400 mbar when the aircraft was below 7.3 km, and 150
283   mbar above 7.3 km. The residence time of the air inside the optical cavities is estimated to be
284   0.5 s.
285
286   The measured absorption spectrum is fit to a linear combination of literature or reference
287   spectra of absorbing gas-phase species and a polynomial to account for drifts in the cavity
288   stability or light source intensity, as detailed by Min et al. (2016), using a Levenberg-
289   Marquardt least-squares fitting algorithm. For the 365 nm channel, those species are NO_2,
290   HONO, O_4, and a 4th order polynomial. For the 455 nm channel, those species are NO_2,
291   glyoxal, methylglyoxal, H_2O, and O_4, as well as a 0th order polynomial, though only NO_2 is
292   presented here. The algorithm uses reference spectra for NO_2 and glyoxal, as measured in the
293   field, scaled linearly to the literature spectra of Vandaele et al. (1998) at 296 K and Volkamer
294   et al. (2005) at 294 K, respectively. The literature spectra from Stutz et al. (2000), Meller et
295   al. (1991), Harder & Brault, (1997), and Keller-Rudek et al. (2013) are used for HONO,
296   methylglyoxal, H_2O, and O_4, respectively. The fitting range was 438 – 467 nm for the 455
297   nm channel, and 362 – 387 nm for the 365 nm channel. No structure was observed in the fit

298 residuals. Because the 455 nm channel has higher precision, only those NO_2 data are
299 presented here, although the two channels agree to within 3%. The data are averaged to 1 s.
300 The reported uncertainties are $\pm$ (9% + 0.6 ppbv) for HONO and $\pm$ (5% + 0.26 ppbv) for
301 NO_2, representing the accuracy and 2-sigma precision in 1 second.
302
303   2.2.5   Iodide-Adduct Chemical Ionization Mass Spectrometry (HONO)
304
305 HONO was measured using a modified commercial time of flight chemical ionization mass
306 spectrometer (TOF CIMS, Aerodyne Research, Inc.; Lee et al., 2014; Veres et al., 2020).
307 Trace gases are ionized by mixing ambient air with reagent ions made in flight, and the
308 resulting product ions are detected. Ions are separated by mass-to-charge ratio (m/z) using a
309 time-of-flight mass spectrometer with a resolving power of 5000 m/Δm and a range of mass
310 to charge ratio up to 494 m/z. Spectra were obtained at a 25 kHz repetition rate, and then
311 averaged to 1 s. High resolution peak fitting was performed on the spectra, using over 500
312 known masses. Reagent ions were formed by flowing 1 slpm N_2 through a temperature
313 controlled CH_3I permeation tube followed by a 20 mCi ^{210}Po radioactive source. Two reagent
314 ions are generated: Iodide ions (I$^-$) are formed in the radioactive source, and iodide-water
315 clusters (I$\cdot H_2O$) are formed when I$^-$ reacts with water in the ion-molecule reactor (IMR). In
316 the IMR, the reagent ions cluster with analyte gases to form stable iodide adducts. The IMR
317 was controlled at 40 mbar pressure to reduce the effects of secondary ion chemistry that
318 increase at higher pressures.
319
320 Ambient air was sampled through a mass flow controlled (6 slpm) heated perfluoroalkoxy
321 (PFA) inlet (70 cm length, 0.64 cm inner diameter). A pressure control region upstream of a
322 critical orifice at the entrance to the IMR was maintained at 140 mbar, so that a constant flow
323 of 1.2 slpm ambient air entered the IMR to mix with the 1 slpm ion source flow. A small
324 nitrogen flow of about 20 sccm containing water vapor was added directly into the IMR
325 region and controlled to maintain a measured I$\cdot H_2O$:I$^-$ cluster ratio of 50 $\pm$ 2%, in order to
326 maintain constant detection sensitivity. The reagent ion signals during FIREX-AQ were
327 typically 2 MHz for I$\cdot H_2O$ and 4 MHz for I$^-$, and they were stable as a function of aircraft
328 altitude. In the most concentrated fire plumes with CO over 7 ppm, the abundance of
329 reactants reduced the reagent ion signals by up to 15%. The product cluster ions were
330 normalized by the iodide (I$\cdot H_2O$) signals to account for changes in reagent ions. The
331 instrument background signal was determined inflight by overflowing the inlet with scrubbed
332 ambient air for 30 seconds every 10 minutes through a port located 2 cm downstream of the
333 inlet entrance. Calibrations with Cl_2 and HNO_3 permeation sources were performed hourly in
334 flight to diagnose the stability of instrument sensitivity. The standard deviation of in flight
335 calibrations was typically 10%.
336
337 HONO was detected as a cluster with I$^-$ that has a mass to charge ratio of 173.90575 m/z.
338 Contributions from the ^{13}C isotope of formic acid at 173.91342 m/z are not completely mass
339 resolved but are accounted for using high resolution peak fitting and isotope ratios based on
340 the formic acid signal at its most abundant isotope. We know of no other contributions to the

341 signal at the mass used for HONO detection, consistent with previous studies (Neuman et al.,
342 2016). The background HONO signals were typically equivalent to a mixing ratio of 40 ppt,
343 and these were subtracted from the total signal to determine ambient HONO. Sensitivity to
344 HONO was determined in the laboratory, using a tunable, calibrated HONO source that uses
345 HCl reactions on humid $NaNO_2$ to generate HONO (Lao et al., 2020). The output was
346 calibrated spectroscopically using the NOAA ACES instrument (Min et al., 2016). The
347 absolute sensitivity to HONO was 3.4 ion counts/s/pptv for typical conditions. Sensitivities
348 normalized by the reagent ions are used to determine mixing ratios from the normalized
349 product ion signals. The HONO measurement uncertainty at fixed temperature was ± (15% +
350 3 pptv), where the first term was from the laboratory calibrations and the second was the
351 variability of the in-flight background determinations. The HONO measurement precision
352 was ± 2 pptv for 1-second data. Calibrations and fieldwork conducted subsequent to FIREX-
353 AQ identified a temperature dependence to the CIMS calibration. Section 3.3 below
354 describes this sensitivity in more detail.
355
356   2.2.6 ΣNO_y
357 To determine the extent of budget closure for reactive odd nitrogen species during FIREX-
358 AQ, we compare measured NO_y (see section 2.2.1) with a simplified definition of ΣNO_y as
359 illustrated in the following equation:
360
361 $\Sigma NO_y \approx NO_x + HONO + HNO_3 + pNO_3 + APNs$ (Eq. 2)
362
363 Other nitrogen oxides were also measured during FIREX-AQ but were not included in this
364 equation as they contributed on average less than 7% to the NO_y budget (see section 3.4).
365 Further, including these measurements would have decreased data availability for comparison
366 with the total NO_y measurement by more than 60%. These minor NO_y species are alkene
367 hydroxy nitrates, nitromethane (CH_3NO_2), N_2O_5, $ClNO_2$, and C_1–C_5 alkyl nitrates (Figures S1
368 and S2). Measurements used in Eq. 2 are CL NO_x, CIMS HONO, CIMS HNO_3, HR-AMS
369 pNO_3 and CIMS APNs. These measurements were primarily used because they had better
370 precision. Using LIF NO, CES NO_2 and CES HONO as primary measurements changed the
371 correlation slope between ΣNO_y and measured NO_y by -2%, -6% and 6%, respectively (Table
372 S1). In smoke, using LIF NO, CES NO_2 and CES HONO as primary measurements changed
373 the correlation slope between ΣNO_y and measured NO_y by -1%, -8% and 9%, respectively
374 (Table S1).
375
376   •   Observations of HNO_3, HCN, and hydroxyl nitrates produced from the oxidation of
377   ethane, propene, butane, and isoprene were made by the California Institute of
378   Technology Chemical Ionization Mass Spectrometer (CIT-CIMS) compact time-of-
379   flight (cToF, TofWerk/Caltech) sensor using CF_3O^- ion chemistry (Crounse et al.,
380   2006). In short, a large flow of ambient air (about 40 m^3 s^{-1}) was rapidly brought into
381   the aircraft through a Teflon coated glass inlet (warmed slightly above ambient
382   temperature), where it was subsampled, diluted with dry N_2, reacted with CF_3O^-, and
383   underwent subsequent product ion analysis by time-of-flight mass spectrometry. The

384   HF•NO_3^- (m/z 82) product ion is used to quantify HNO_3. The HCN and hydroxy

385   nitrates are detected as cluster ions. Laboratory-generated, T-dependent and water-

386   dependent calibration curves were performed to produce ambient mixing ratios from

387   raw signals for HNO_3 and hydroxy nitrates The HCN sensitivity is tracked in situ

388   based on the continuous addition of isotopically labeled $H^{13}C^{15}N$ into the instrument

389   from a custom-made gravimetrically based compressed gas cylinder. In-flight

390   instrumental zeros were performed every ~15 minutes using dry N_2 and ambient air

391   passed through $NaHCO_3$-coated nylon wool. Continuous data, with the exception of

392   zero and calibration periods, are reported with 1Hz frequency. The uncertainties for

393   HNO_3, HCN, and hydroxy nitrates are ± (30% + 50 pptv), ± (25% + 70 pptv), and ±

394   (25% + 3 pptv), respectively.

395

396   • Particulate nitrate (pNO_3) was measured with a high-resolution time-of-flight AMS

397   (HR-AMS, Aerodyne Research, Inc., Billerica, MA, USA). The HR-AMS measured

398   submicron ($PM_{0.9}$; calibrated in the field as described in Guo et al., 2021) aerosol

399   composition at high time resolution (0.1−1 s) by flash vaporization of the aerosol, 70

400   eV electron ionization of the volatilized gas phase and subsequent analysis by mass

401   spectrometry (Canagaratna et al., 2007; DeCarlo et al., 2006). pNO_3 is detected in the

402   HR-AMS as the sum of $H_xNO_y^+$ ions (mostly NO^+ and NO_2^+). Typical 1 s detection

403   limits for pNO_3 were about 90 ng sm^{-3} (30 pptv) for urban/background conditions.

404   Given the size cut in the HR-AMS instrument, pNO_3 does not include coarse nitrate

405   from the reaction of HNO_3 with sea salt or dust aerosol. It does include particulate

406   organic nitrates (p$RONO_2$; Day et al., 2021; Farmer et al., 2010), which are speciated

407   using the algorithm described in Fry et al. (2013) and Day et al. (2021). Likewise,

408   particulate aryl nitrates such as nitrocatechol also contribute to the total pNO_3 signal

409   (Guo et al., 2020). Nitrocatechol was also characterized by extractive electrospray

410   ionization time-of-flight mass spectrometry (EESI-MS; Pagonis et al., 2021) and

411   positive matrix factorization and tracer analysis suggests that total aryl nitrates could

412   be 3–7 times the concentration of nitrocatechol.

413

414   • APNs were measured using a thermal dissociation – chemical ionization mass

415   spectrometer (TD-CIMS) method. The CIMS instrument used during the FIREX-AQ

416   campaign was similar to that described in Slusher et al. (2004) and Lee et al. (2020).

417   Briefly, ambient air is sampled into the TD-CIMS through heated Teflon tubing at a

418   temperature of approximately 150℃ to thermally dissociate APNs. The thermal

419   dissociation region was maintained at a constant pressure of 60 torr using a

420   commercial pressure controller (MKS 640) to minimize negative interference due to

421   NO, NO_2 and radical-radical reactions. In-flight calibrations were performed by

422   continuous addition of isotopically labeled peroxyacetyl nitrate (PAN) standard

423   quantified as acetate ion (61 m/z; $C^{13}H_3C^{13}(O)O^-$) in the TD-CIMS. NO was

424   periodically added to the inlet (~10 ppm) to react away peroxyacyl radicals and thus

425   to measure the instrument background signal. APNs species measured during FIREX-

426   AQ include PAN, acryloyl peroxynitrate (APAN), propionyl peroxynitrate (PPN), and

427   peroxybutyryl nitrate (PBN) with an uncertainty of 20%, 30%, 30% and 30%,
428   respectively.

429

430   • Nitromethane (CH_3NO_2), along with other volatile organic compounds (VOCs), was
431   measured by proton-transfer-reaction time-of-flight mass spectrometry (PTR-ToF-
432   MS; Gkatzelis et al., in prep). The PTR-ToF-MS sampled VOCs at 5Hz through short
433   (1 m) heated inlet. Periodically, instrument backgrounds were determined by passing
434   ambient air through a platinum catalyst heated to 350°C. The instrument response to
435   VOCs was calibrated by gravimetrically prepared standards or by liquid calibration,
436   as described by Gkatzelis et al. (2021). CH_3NO_2 mixing ratios were determined by
437   liquid calibration with an uncertainty of 30%.

438

439   • N_2O_5 was detected as a cluster with I^- at mass 234.88574 m/z. Sensitivity was
440   determined by standard addition laboratory calibrations, with N_2O_5 generated by
441   reacting a NO_2 calibration standard with O_3 (Bertram et al., 2009), and quantified
442   using cavity ring down NO_y measurements (Womack et al., 2017). For typical
443   operating conditions during FIREX-AQ, N_2O_5 sensitivity was 70 ion counts/s/ppt.
444   N_2O_5 was measured with $\pm$ (15% + 2 pptv) accuracy and 0.1 pptv precision for 1
445   second data. Iodide ions cluster with a DMS oxidation product, hydroperoxymethyl
446   thioformate (HPMTF), that has a mass only 0.0074 amu greater than N_2O_5, and these
447   two molecules cannot be completely resolved spectrometrically with the resolution
448   (m/Δm = 5000) of this instrument (Veres et al., 2020). For these measurements over
449   the continent, the contribution from HPMTF to the signal at the iodide N_2O_5 cluster is
450   assumed to be negligible.

451

452   • C_1–C_5 alkyl nitrates were measured by the NOAA integrated whole air sampling
453   system with off-line analysis by gas chromatography-mass spectrometry (iWAS/GC-
454   MS as described in Lerner et al. (2017)). There were 142 iWAS samples collected
455   over the LA Basin with an average fill time of 5.2 ± 0.7 seconds. There were 897
456   wildfire samples and 467 eastern fire samples with average fill times of 7.6 ± 1.1 and
457   4.5 ± 0.8 seconds, respectively. Due to the relatively fast fill times and targeted, on-
458   demand sampling capabilities of the iWAS, 88% and 74% were "full smoke" samples
459   for wildfire and eastern fire samples, respectively. All samples were analyzed in the
460   NOAA Chemical Science Laboratory within 213 hours of sample collection with an
461   average sample age of 87 ± 34 hours between sample collection and sample analysis
462   for FIREX-AQ.

463

464   2.2.7   Integrated Cavity Output Spectroscopy (CO)
465 CO was measured using a modified commercial off-axis ICOS instrument (Los Gatos
466 Research (LGR) N_2O/CO-30-EP; Arévalo-Martínez et al., 2013; Baer et al., 2002) at 4.566
467 μm. The commercial instrument has two flow paths, a slow flow path with cavity pressure
468 controlled by an internal proportional valve, and a parallel high flow path with a needle valve
469 to control pressure. The instrument was modified to use only the high flow path, but with an

470 automatic cavity pressure controller. The needle valve was removed from the flow path in
471 favor of a Piezo proportional valve (Horiba Stec UR-Z732M) located near the inlet.
472
473 Air was sampled from a ram-air intake inlet through 0.64 cm (outside diameter) stainless
474 steel tubing. Cavity pressure was maintained at 85.0 ± 0.2 Torr in flight. Immediately inside
475 the fuselage, two CO (and N_2O) calibration gas standards known to within ±0.4 ppb CO were
476 regularly delivered to the inlet line during flight to evaluate instrument sensitivity between
477 58.4 and 993.3 ppb CO (both ICOS-CO and TDLAS-CO mixing ratios are reported as dry air
478 mole fractions). The calibration standards were added to displace ambient air and overflow
479 the inlet, and were calibrated before and after the project using standard tanks tied to the
480 World Meteorological Organization CO_X2014A scale from the NOAA Global Monitoring
481 Laboratory (Hall et al., 2007; Novelli et al., 1991). The 1-sigma variability of the slope and
482 intercept of all in-flight calibrations was 0.6% and 0.9 ppb, respectively. A third calibration
483 standard, referred to as a "target" (Peischl et al., 2010), was regularly introduced to the inlet
484 between calibrations and treated as an unknown to evaluate long-term instrument
485 performance. The retrieved value of 109 in-flight targets during FIREX-AQ was 301.6 ± 1.0
486 ppb CO compared with the calibrated value of 301.1 ± 0.4 ppb. The 1-Hz precision of the
487 measurement in flight is estimated to be 0.4 ppb.
488
489 After the campaign, the H_2O measurement was calibrated using a MBW 373LX chilled-
490 mirror hygrometer (MBW Calibration AG; Rollins et al., 2020). The H_2O measurement is
491 estimated to have an uncertainty of $\pm$ (50 ppmv + 4%), and was used to convert the CO
492 measurement to a dry air mole fraction. The uncertainty of the dry air mole fraction of CO is
493 estimated to be $\pm$ (2.0 ppb + 2%) for mixing ratios below 1 ppm.
494
495   2.2.8   Tunable Diode Laser Absorption Spectroscopy (CO)
496 Carbon Monoxide (CO) was measured by tunable diode laser absorption spectroscopy
497 (TDLAS) using the DACOM (Differential Absorption Carbon monOxide Measurement)
498 instrument (Sachse et al., 1987). The TDLAS instrument configuration used during FIREX-
499 AQ also included channels for measurements of methane (CH_4) and carbon dioxide isotopes
500 ($^{12}CO_2$ and $^{13}CO_2$). This instrument utilizes three single-mode tunable diode lasers, with CO
501 measured using a quantum cascade laser (QCL) at approximately 4.7 μm. The three
502 individual mid-infrared laser beams were combined by the use of dichroic filters and directed
503 through a small volume (0.3 liter) Herriott cell enclosing a 36-meter optical path. After
504 exiting the Herriott cell, the beams were spectrally separated and directed to individual
505 HgCdTe (MCT) detectors.
506
507 The lasers were operated in a wavelength-modulated mode, each at an independent
508 frequency, and line-locked to the centers of the species' selected absorption lines. Lines were
509 selected to provide both good sensitivity and good isolation from any potential spectral
510 interferences. Detector signals were demodulated at twice the lasers' modulation frequencies
511 (2F detection), and normalized by average detected laser intensity.
512

513　Ambient air was sampled through an inlet probe, compressed, and passed through a
514　permeable membrane dryer to remove water vapor prior to being introduced into the Herriott
515　cell. Due to the need for very fast time response during FIREX-AQ, the instrument was
516　operated with a flow of approximately 14 slpm with the Herriott cell at a pressure of
517　approximately 67 mbar. The resulting time response, verified with a fast-acting valve, was
518　faster than 0.2 s. Data were reported at both 0.2 s and 1 s timesteps.
519
520　The TDLAS instrument was calibrated using the same gas standards as for the ICOS
521　instrument, nominally with a 4-minute period, but often advanced or delayed in time to avoid
522　calibrating during fire plume encounters. Calibrations provided both slope and intercept
523　values tying signals to species concentrations. The very large CO concentrations encountered
524　necessitated post-campaign correction calibrations to account for response nonlinearity.
525
526　Post-campaign analysis of the TDLAS CO data indicated that measurement precision (1σ)
527　was approximately 0.1% at 1 s and 0.14% at 0.2 s. Accuracy was dependent on CO mixing
528　ratio, and varied from 2% to 7%.
529
530　　　　2.2.9　H_2O
531　H_2O was measured using the NASA diode laser hygrometer, an open-path infrared absorption
532　spectrometer that uses a laser locked to one of three water vapor absorption features near
533　1.395 μm, depending on the abundance of water vapor (Diskin et al., 2002; Podolske et al.,
534　2003). H_2O mixing ratios were determined with an uncertainty of 5%.
535
536　　　　2.2.10　Smoke age
537　The age of smoke from emission to sampling by the aircraft was determined from an
538　ensemble of upwind trajectories from the aircraft (Holmes et al., 2020). Trajectories were
539　computed with HYSPLIT (Stein et al., 2015) using three meteorological datasets (HRRR,
540　NAM CONUS Nest, and GFS 0.25°). In each of the three trajectories, the advection time was
541　determined from the point where the trajectory most closely approached the source fire. The
542　age also includes plume rise time from the surface to trajectory altitude, which was estimated
543　with a mean rise time of 7 ± 4 m s^{-1} (Lareau et al., 2018). Trajectories and ages that were
544　grossly inconsistent with smoke transport patterns seen in geostationary satellite images were
545　excluded from further analysis. The ensemble of age estimates was then averaged to provide
546　a best estimate of smoke age. The median uncertainty in smoke age is about 27%, as
547　determined by the sum in quadrature of the spread among the ensemble of estimates, the
548　uncertainties in the updraft speed, the fire location and the wind speed, and uncertainties in
549　the model.
550
551　　　　2.3 Methodology
552　This study focuses on comparing the different techniques used for the measurements of one
553　or several reactive nitrogen species as well as CO during FIREX-AQ. Here we compare both
554　archived 1 s data (https://www-air.larc.nasa.gov/missions/firex-aq/index.html) and the plume-
555　integrated data. Plume-integrated data are obtained from integrating the 1Hz data of a given
556　measurement over a smoke plume transect. A smoke plume transect was identified using the

557   time period between a CO and/or black carbon (BC) increase above a local background value
558   (beginning of the plume transect) and the CO and/or BC decrease back to a background value
559   (end of the plume transect). Background values on either side of a plume were different for
560   some fires in spatially heterogeneous source regions. Note that any 10 s period of background
561   air, even if experienced during a single smoke plume transect, was sufficient to mark the end
562   of one transect and the start of the next. All 1Hz data were time-aligned prior to comparison
563   by synchronizing features in the time series of each species. Time shifts were typically less
564   than 4 seconds. Some disagreement between measurement techniques is expected due to the
565   rapid variations sampled during FIREX-AQ, particularly when those variations occur faster
566   than the measurement period and/or with greater spatial heterogeneity than the distance
567   between the sampling locations on a large aircraft that can reach 25m in some cases.
568   Comparisons in this manuscript are not blind as all PIs had access to other instruments
569   measurements throughout the campaign.
570
571   We first calculated the slope of the linear least-squares (LLS) orthogonal distance regression
572   (ODR; Boggs et al., 1987) to characterize the percent difference between measurements of a
573   pair of instruments weighted by the inverse of the instrument precision. Here, we used a
574   mixing ratio-independent instrument precision that corresponded to the 1σ precision in clean
575   air. Weighting the fit by this term, rather than a more accurate but labor-intensive mixing-
576   ratio-dependent precision, tend to overweight the highest measured mixing ratios. The slope
577   and intercept resulting from the ODR regression analysis provide a measure of systematic or
578   species-dependent instrumental biases. Additionally, we calculated the difference between a
579   given pair of measurements. The difference, noted $\Delta Y_{X1\text{-}X2}$ where X1 and X2 are the two
580   measurement techniques for detection of the Y species, provides an understanding of the
581   temporal evolution and environmental dependency of instrumental discrepancies. Note that
582   the regression analysis yields slightly different information than the calculation of the
583   difference: while the former is weighted more by fire plumes, where mixing ratios were
584   greatest, the latter is weighted more by background conditions, where most of the
585   measurements took place. Unless specified otherwise, all data available (i.e., both
586   background and fire smoke data) were included in the following comparisons. We also
587   calculated the fractional error (FE = $\Delta Y_{X1-X2}/Y_{avg}$ where $Y_{avg} = (Y_{X1} + Y_{X2})/2$) between pair
588   of instruments using specifically fire smoke data to minimize measurements below
589   instrument detection limits (Figures S3 and S4). In the following sections, combined
590   instrument uncertainties were calculated by adding in quadrature individual instrument
591   uncertainties.
592
593   **3   Flight data comparisons**
594   3.1 <u>NO</u>
595   3.1.1   Campaign-wide comparison
596   The 1Hz data comparison between the CL and LIF instruments is shown in Figure 2. The
597   overall comparison slope (± combined instrument uncertainties) is 0.98 ± 0.08 (R^2 = 0.93)
598   with an intercept of −2 ± 0 pptv (Figure 2a). Figures 3a and 4a show the two instruments'
599   response in smoke from a wildfire and an eastern fire, respectively. While the NO signals
600   track each other remarkably well, there is a difference in time response that is typical of the

601 entire campaign. Figure S5 shows an expanded view of 10Hz NO and CO measurements in a
602 partial smoke plume transect, including the transition from smoke to background air
603 sampling. The NO signal in the CL instrument exhibits less structure than in the LIF
604 instrument and a tail following the plume-to-ambient air transition. These tails were
605 commonly observed during this transition. This effect in the CL instrument may partly
606 explain the elevated scatter below the 1:1 line in Figure 2b. Integrating the NO signal across
607 plume passes reduces the scatter due to different instrument time response: the regression
608 analysis of smoke plume-integrated NO mixing ratios yields a slope of 0.99 ($R^2 = 0.95$) for
609 the whole dataset (Figure 2c).
610
611 A histogram of the absolute difference between LIF and CL (ΔNO_{LIF-CL}) is shown in Figure
612 5a. 90% of the values were between –44 and 43 pptv, and the whole dataset is normally
613 distributed around 0 ± 0 pptv (central value of the Gaussian fit and standard deviation).
614 ΔNO_{LIF-CL} exhibits no significant correlation with NO and H_2O mixing ratios, which suggests
615 that there was no systematic bias between the two instruments over a wide range of NO
616 mixing ratios and environmental conditions (Figures S6a and 6a). Similar slopes and
617 intercepts were obtained when separately comparing NO measurements during the wildfire,
618 eastern fire, and LA Basin sampling periods (Figures 2b and S7).
619
620   3.1.2   Literature aircraft NO measurement comparisons
621 Overall, the comparison between the two NO instruments shows an agreement within stated
622 uncertainties. While the single-photon LIF detection of NO is a new technique that was
623 evaluated for the first time during FIREX-AQ (Rollins et al., 2020), there are several studies
624 that compared CL detection of NO to other measurement techniques during airborne field
625 campaigns. The Global Tropospheric Experiment Chemical Instrumentation Test and
626 Evaluation (GTE-CITE) was designed in the 1990's to intercompare airborne measurement
627 techniques for trace species including NO, NO_2 and CO. Comparison of two CL instruments
628 and a two-photon LIF instrument showed agreement when NO mixing ratios were higher
629 than 50 pptv, but pointed out periods of disagreement when NO mixing ratios were lower
630 than 20 pptv (Gregory et al., 1990; Hoell et al., 1987). The Deep Convective Clouds &
631 Chemistry (DC3) experiment in 2012 allowed for side-by-side comparison of instruments
632 aboard two aircrafts at two level flight legs (7 and 12 km) for flight periods spanning 20–30
633 minutes. Pollack et al. (2016) showed that these NO measurements from two CL instruments
634 agreed within 2% for NO mixing ratios up to 1 ppbv. More recently, Sparks et al. (2019)
635 reported an intercomparison of several NO_y species measurements, including NO, from the
636 Wintertime Investigation of Transport, Emissions, and Reactivity (WINTER) airborne
637 experiment over the Northeast US in 2015. During WINTER, NO measured by CRDS and
638 CL differed on average by 16 % across all flights, which is outside of the combined
639 instrument uncertainties. CL measurements were more consistent with an independent
640 calculation of NO based on a photostationary state assumption.
641
642   3.2 $\underline{NO_2}$
643   3.2.1   Campaign-wide comparison

644   Three instruments measured NO_2 mixing ratios during FIREX-AQ using CL, CES and LIF

645   detection techniques. The 1Hz data comparison between all three instruments is shown in

646   Figure 7. We find that the LIF and CES overall comparison yields a slope (± combined

647   instrument uncertainties) of 1.03 ± 0.08 ($R^2 = 0.98$), well within the combined instrument

648   uncertainties of 8% (Figure 7c). However, we find that comparing either the LIF or CES

649   instruments to the CL instrument results in correlation slopes (± combined instrument

650   uncertainties) ranging from 0.88 ± 0.12 to 0.90 ± 0.11 ($R^2 = 0.97$), on the upper limit of the

651   8–11% combined uncertainties for each pair of instruments (Figures 7a and b). The higher

652   NO_2 mixing ratios measured by the CL instrument are further illustrated in the time series in

653   Figures 3b and 4b, and is consistent with a calibration error in one or all instruments, or an

654   interference from another species in the CL instrument. However, it is unlikely that the

655   difference between CL NO_2 and other NO_2 measurements was due to a calibration issue. If

656   so, the CL NO measurement, which was calibrated using the same standard as for the CL

657   NO_2 measurement, would also have been 10-12% higher than the NO LIF measurement

658   (which was calibrated using an independent standard). This was not the case during FIREX-

659   AQ (see section 3.1). HONO is a known source of interference in measured NO_2 by

660   instruments that use photolysis in the near-UV region (Pollack et al., 2010). However, this

661   interference was determined to be low (less than 5% of HONO concentration; typical HONO

662   to NO_2 ratios ranged between 0.2–0.4 during FIREX-AQ) following laboratory tests using a

663   HONO calibration source (Lao et al., 2020), and the NO_2 measurement by CL was corrected

664   for it. Additionally, we did not find a correlation between either $\Delta NO_{2CES-CL}$ or $\Delta NO_{2LIF-CL}$

665   and HONO mixing ratios. There was better agreement between the CL and the other two

666   instruments when sampling the wildfires (slopes of 0.91) than the eastern fires (slopes of 0.75

667   and 0.87 for the LIF and CES, respectively) (Figures 7d and e). Similarly, the agreement

668   between the CES and the LIF instruments was near perfect during the first period (slope of

669   1.00), but worse during the latter period (slope of 1.13; Figure 7f). Note that the LIF

670   instrument did not report data for three flights out of seven during the eastern fires sampling

671   period. The increased difference may be caused by the physical distance between instrument

672   inlets combined with higher spatial heterogeneity of trace gases in the smaller and thinner

673   eastern fire plumes, although higher mixing ratios of a potential interferent may still exist.

674   Non-acyl peroxynitrate species such as pernitric acid (HO_2NO_2) and methyl peroxy nitrate

675   (MPN) can be abundant in smoke plumes and interfere with NO_2 measurements (Browne et

676   al., 2011; Nault et al., 2015). This interference is the result of the thermal dissociation of

677   HO_2NO_2 and MPN in heated inlets and sampling lines, and impact differently each

678   instrument depending on their flush time. During FIREX-AQ, the CES and CL instruments

679   had similar flush time of about 750ms meaning that the thermal decomposition of non-acyl

680   peroxynitrates is unlikely to explain the 10–12% higher NO_2 signal in the CL instrument.

681   Further, $\Delta NO_{2CES-CL}$ or $\Delta NO_{2LIF-CL}$ did not depend on altitude or outside temperature, which

682   also suggests little influence from thermally labile species. Nitrated phenolic compounds

683   can be abundant in aged smoke (Decker et al., 2021), and have large UV cross sections (Chen

684   et al., 2011). They are unlikely to contribute to the interference as their NO_2 photolysis

685   quantum yields are very low. Nevertheless, further laboratory work on the NO_2 interference

686   of such species in photolytic converters is of interest. The agreement between all three

687 instruments for individual flights was generally within combined instrument uncertainties,
688 but with some variability (Figures S8–S10).
689
690 Histograms of the absolute difference between CES, LIF and CL ($\Delta NO_{2LIF-CL}$, $\Delta NO_{2CES-CL}$
691 and $\Delta NO_{2CES-LIF}$) are shown in Figures 5b–d. 90% of $\Delta NO_{2LIF-CL}$, $\Delta NO_{2CES-CL}$ and ΔNO_{2CES-}
692 $_{LIF}$ values were between –298 and 338 pptv, –469 and 302, and –576 and 393 pptv,
693 respectively, and all are normally distributed around the central value of the Gaussian fit of
694 0.038 ± 0.001, –0.052 ± 0.001, and –0.071 ± 0.001, respectively. $\Delta NO_{2LIF-CL}$, $\Delta NO_{2CES-CL}$
695 and $\Delta NO_{2CES-LIF}$ exhibit no significant trend with H_2O mixing ratios (Figures 6b–d), yet
696 $\Delta NO_{2LIF-CL}$ and $\Delta NO_{2CES-CL}$ were weakly (R^2 = 0.36 and 0.31, respectively) correlated with
697 the absolute NO_2 mixing ratio (Figures S6b and d).
698
699   3.2.2   Literature aircraft NO_2 measurement comparisons
700 Previous comparisons of NO_2 airborne measurements often show periods of disagreement
701 between instruments, although there were some occasions where instruments agreed within
702 stated uncertainties. During the GTE-CITE experiment, the comparison of NO_2
703 measurements using a two-photon NO LIF system with laser photolysis of NO_2 to NO with a
704 CL detector equipped with a xenon arc lamp for NO_2 photolysis into NO showed agreement
705 within 30–40% (Gregory et al., 1990). Pollack et al. (2016) showed that two NO_2
706 measurements, both using CL but each in a different aircraft, agreed within 28% during the
707 DC3 campaign. During WINTER, NO_2 measurements by CRDS and LIF agreed with an
708 average proportional bias of 2% across all flights – well within combined uncertainties
709 (Sparks et al., 2019). During SENEX, three techniques were used to measure NO_2: a CRDS
710 instrument, a CES instrument and a CL instrument. The agreement between CRDS and CES
711 measurements with the CL technique was on average 6 and 10% (Warneke et al., 2016).
712
713   3.3 <u>HONO</u>
714   3.3.1   Campaign-wide comparison
715 The 1Hz data comparison between the CES and the CIMS instruments is shown in Figure 8,
716 and timeseries of HONO measurements in wildfires and eastern fires are shown in Figures 3c
717 and 4c, respectively. The correlation between the CES and CIMS was very high in each
718 plume transect (Figures 3c and 4c), but the overall comparison yielded a slope (± combined
719 instrument uncertainties) of 1.80 ± 0.16 (R^2 = 0.77) and an intercept of –0.12 ± 1.10 ppbv
720 (Figure 8a). Integrating across plume transects yielded a slope of 1.34 ± 0.16 (Figure 8c). The
721 CIMS consistently reported less HONO than the CES in smoke plumes, and the average
722 slope between the two measurements was considerably greater during the eastern fires
723 compared to the wildfires (Figures 8b and S9). However, flight averages of the absolute
724 difference between the two measurements ($\Delta HONO_{CES-CIMS}$) ranged between –332 and 245
725 pptv throughout the campaign and were similarly scattered around zero during the two
726 different time periods (Figure S11). A histogram of $\Delta HONO_{CES-CIMS}$ is shown in Figure 5e.
727 90% of the values were between –965 and 880 pptv, and the whole dataset is normally
728 distributed around the central value of the Gaussian fit (± standard deviation) of –119 ± 2
729 pptv. $\Delta HONO_{CES-CIMS}$ exhibits no significant slope with HONO (Figure S6e). While the
730 deployment out of Salina was operated under noticeably more humid conditions (H_2O ranged

731 from 0.002 to 2.944%) than out of Boise (H_2O ranged from 0.004 to 1.479%), we find no
732 significant correlation between $\Delta HONO_{CES-CIMS}$ and H_2O mixing ratios (Figure 6e).
733
734 However, further laboratory studies, field measurements, and examination of this comparison
735 has revealed that the CIMS sensitivity to HONO is reduced when the instrument reaches
736 temperatures greater than 30°C (Figure S12). This sensitivity dependence on temperature
737 does not affect all compounds measured by the CIMS, and the sensitivity to Cl_2 and HNO_3
738 used for in-flight calibrations was independent of instrument temperature. The aircraft cabin
739 temperature was greatest during the eastern agricultural flights, when the CIMS instrument
740 temperatures were often 40°C and far greater than the typical 25°C instrument temperatures
741 in the laboratory when the CIMS HONO sensitivity was determined. As a consequence, the
742 reported CIMS HONO values were spuriously low, especially during the eastern fires, and
743 particularly later in flights when the aircraft temperatures were greatest. This intercomparison
744 has yielded new insights into the CIMS HONO detection sensitivity, and future work will
745 identify and implement appropriate corrections to this measurement (Robinson et al. 2022).
746
747   3.3.2   Literature aircraft and ground HONO measurement comparisons
748 The interpretation of literature suggest that HONO measurements are notoriously difficult
749 due to the potential for artifacts associated with inlet surfaces as well as interferences
750 associated with some methods (e.g., Kleffmann et al., 2006; Xu et al., 2019). Past ground-
751 based intercomparisons often revealed significant discrepancies in HONO measurements. For
752 example, six ground-based HONO measurement techniques including a CIMS instrument
753 were compared during the Study of Houston Atmospheric Radical Precursors (SHARP)
754 campaign in 2009 (Pinto et al., 2014). While three out of six of these techniques agreed
755 within 20%, larger deviations were found when the other three instruments were considered
756 and attributed to the physical separation of these instruments. Three different techniques,
757 including a CIMS instrument, were used to measure HONO in the urban area of Shanghai,
758 China (Bernard et al., 2016). The percent difference between these measurements ranged
759 from 27 to 46%. In 2019, six HONO measurement techniques were again compared in a
760 Chinese urban area, this time in Beijing, and included a CIMS instrument as well as two
761 broadband cavity enhanced absorption spectrometers (BBCEAS) (Crilley et al., 2019).
762 Percent differences up to 39% were observed during this intercomparison and again
763 attributed to the physical distance separating inlets coupled to high spatial heterogeneity of
764 HONO mixing ratios. Airborne measurements of HONO by CIMS and CES were made
765 during the Southeast Nexus Experiment (SENEX), and the CES instrument was
766 approximatively 25% higher than the CIMS instrument (Neuman et al., 2016).
767
768   3.4 $\underline{NO_y}$
769   3.4.1   Campaign-wide comparison
770 The 1Hz data comparison between the total NO_y measurement by CL and ΣNO_y is shown in
771 Figure 9. ΣNO_y definition is given by Eq. 2 (see section 2.2.6). C_1–C_5 alkyl nitrates and other
772 minor NO_y species (including $ClNO_2$, N_2O_5, CH_3NO_2, and alkene hydroxy nitrates)
773 contributed less than 7% of the NO_y budget on average and were not included in ΣNO_y

774   (Figure 10). Based on comparisons of HR-AMS pNO_3 with on-board filters collecting
775   aerosols with a size cut around 4μm (Brock et al., 2019; Dibb et al., 2002), coarse mode
776   particulate nitrate did not significantly contribute to the total NO_y budget during FIREX-AQ.
777   Additionally, coarse mode particulate nitrate was not measured by either the HR-AMS or the
778   NO_y inlet in the CL instrument and therefore does not contribute to the intercomparison
779   presented here. The overall comparison yielded a slope (± combined instrument
780   uncertainties) of 1.00 ± 0.25 (R^2 =0.98) and an intercept of −0.52 ± 0.01 ppbv (Figure 9a).
781   The regression analysis of smoke plume-integrated NO_y mixing ratios yields a slope of 1.00
782   (R^2 = 0.99) for the whole dataset (Figure 9c). Comparison ΣNO_y to CL NO_y in fresh (<1h
783   since emission) and aged (>1h since emission) smoke during the wildfires sampling period
784   showed similar agreement (slopes of 0.98 and 1.05, respectively) despite the chemical
785   evolution of NO_y species, highlighted by the different proportion of those species to the NO_y
786   balance (Figure S13). Including minor NO_y species (i.e., $ClNO_2$, N_2O_5, CH_3NO_2, and alkene
787   hydroxy nitrates) in the ΣNO_y had little effect on the correlation between ΣNO_y and CL NO_y
788   and resulted in a slope of 1.02 ± 0.25 (R^2 =0.94) and an intercept of −0.68± 0.01 ppbv (Figure
789   S14).
790
791   Despite this correlation, two modes are apparent in the overall distribution of the absolute
792   difference ($\Delta NO_{yCL–Sum}$) between ΣNO_y and the total NO_y measurement (Figure 5f). The first
793   mode is distributed around −0.068 ± 0.001 ppbv (central value of the first mode of the
794   Gaussian fit), while the second is distributed around an average value of 0.158 ± 0.009 ppbv
795   (central value of the second mode of the Gaussian fit). Separating the comparison into three
796   time periods reveals that this two-mode distribution of $\Delta NO_{yCL–Sum}$ comes from the eastern
797   fires sampling period as well as from the LA Basin flights whereas during the wildfires
798   sampling period $\Delta NO_{yCL–Sum}$ distribution is unimodal (Figure 11).
799
800   Higher ΣNO_y compared to NO_y (first mode) could be explained by (i) a lower conversion
801   efficiency of one or more NO_y species in the CL instrument than estimated in the laboratory,
802   (ii) sampling loss of pNO_3 through the NO_y inlet, and (iii) inaccuracy in one or more of the
803   individual NO_y species measurement techniques. Here, we further investigated the sampling
804   loss of pNO_3 through the CL instrument NO_y inlet using a multistage flow model following
805   the template of the Particle Loss Calculator (von der Weiden et al., 2009). The model
806   calculates aerodynamic losses at each stage of the NO_y inlet and provides the resulting total
807   pNO_3 sampling efficiency (See Section S1 and Figure SA). We find that the main aerosol
808   sampling loss occurs at the NO_y inlet tip orifice (1.0 mm in diameter) due to the inlet
809   orientation (perpendicular to the aircraft flight direction). Additional loss was calculated to be
810   negligible once pNO_3 penetrated the NO_y inlet, meaning that pNO_3 is fully volatilized into
811   NO inside the heated gold catalyst (Miyazaki et al., 2005; see Section S1 and Figure SA).
812   Particle sampling through the NO_y inlet is highly dependent on altitude, air speed (see section
813   S1 and Figure SB) and pNO_3 mass size distribution (Figure 12a). Figure 12b shows the
814   average modeled particle sampling fraction through the NO_y inlet, given as a ratio where a
815   value of 1 means the total pNO_3 is sampled, for each flight during FIREX-AQ. Particle
816   sampling fraction was calculated for three different air speeds for each flight: 40%, 65%, and

817   100% of the aircraft speed. An assumed sampled air speed of 65% that of the aircraft

818   improved the correlation between $\Delta NO_{yCL-Sum}$ and the modeled pNO_3 loss in the inlet (see

819   Section S1 and Figure SB). At that speed, the calculated average particle sampling fraction

820   varied between 0.36 and 0.99 for each flight (Figure 12b). The variability in the ΣNO_y to NO_y

821   correlation slope between aged and fresh smoke (Figure S13a) likely illustrates the non-

822   quantitative sampling of pNO_3 in the NO_y instrument. Indeed, higher ΣNO_y than measured

823   NO_y in aged smoke (slope of 1.05), where pNO_3 is one of the main components of ΣNO_y

824   (Figure S13b), may be explained by the non-quantitative sampling of pNO_3 in the NO_y

825   instrument. In fresh smoke, pNO_3 is a smaller component of NO_y, and non-quantitative

826   sampling of pNO_3 in the CL instrument may have less impact on the comparison (slope of

827   0.98).

828   We calculated the fraction of measured NO_y in smoke initially attributed to pNO_3 that may

829   result from other reactive nitrogen species than those included in the ΣNO_y according to

830   equation 3:

831

832   Missing NO_y fraction = $((1 - \text{particle sampling fraction}) \times pNO_3)\ /\ NO_y$ (Eq. 3)

833   Where particle sampling fraction corresponds to the modeled pNO_3 sampling fraction in the

834   NO_y inlet. We found that missing NO_y accounted for 0–24% of the measured NO_y in smoke

835   (assuming a sampled air speed 65% that of the aircraft; Figure 12b). This additional

836   contribution has a large uncertainty because the model may underestimate pNO_3 sampling

837   through the NO_y inlet due to the large uncertainty when the losses are calculated at high air

838   speed (see Section S1). Further, we used bulk aerosol volume size distributions measured

839   with a Laser Aerosol Spectrometer (LAS; Moore et al., 2021) to derive pNO_3 sampling

840   fractions in Figure 12b as pNO_3 mass size distribution measurements were not available for

841   all flights during FIREX-AQ. At a typical FIREX-AQ sampling altitude of 5 km, the LAS

842   and HR-AMS size distributions can differ by about 10% (See Section S1 and Figure SC),

843   which adds to the uncertainty of the pNO_3 sampling fraction through the NO_y inlet.

844   Correcting for particle sampling through the NO_y inlet still yields an agreement between

845   measured NO_y and ΣNO_y that is within the combined instrument uncertainties of 25%.

846

847   On the other hand, the positive $\Delta NO_{yCL-Sum}$ mode (second mode) may indicate either an

848   inaccuracy in one of the individual NO_y species measurement techniques or an NO_y species

849   not measured. Further, we find that positive $\Delta NO_{yCL-Sum}$ occurred both in smoke (Figure 11d)

850   and in background air (Figure 11c) when sampling the eastern fires and that $\Delta NO_{yCL-Sum}$

851   exponentially decreased with altitude, a pattern also observed during the LA Basin flights but

852   not during the wildfires sampling period (Figure 13b). Note that flight altitude when

853   sampling the wildfires was 4.6 km on average, higher than the altitude average of 0.6 and 1.1

854   km during the eastern fires and the LA Basin flights, respectively. Both water vapor and C_1–

855   C_5 alkyl nitrates (not included in ΣNO_y thus far) were enhanced at lower altitude and may be

856   possible causes for the positive $\Delta NO_{yCL-Sum}$ mode. Alkyl nitrates have been shown to account

857   for a significant fraction of the NO_y budget in past studies (e.g., Fisher et al., 2016; Hayden et

858   al., 2003; Horii et al., 2005). However, we find only a weak correlation between $\Delta NO_{yCL-Sum}$

859 and C_1–C_5 alkyl nitrates during both the wildfires ($R^2 = 0.07$) and eastern fires ($R^2 = 0.08$)
860 sampling periods (Figure 13c). The correlation is stronger ($R^2 = 0.44$) during the LA Basin
861 flights (Figure 13c). Further, we find that C_1–C_5 alkyl nitrates contributed similarly to the
862 NO_y budget when smoke from the wildfires (1.1% on average) and the eastern fires (0.8% on
863 average) was sampled (Figure 10a), while the positive mode in the $\Delta NO_{yCL–Sum}$ distribution is
864 present in the latter period only. H_2O is a known source of interference in most instruments,
865 and its impact on measurements is minimized when an accurate correction can be applied.
866 Increasing $\Delta NO_{yCL–Sum}$ is associated with increasing H_2O mixing ratios in the eastern fires,
867 although the correlation is weak ($R^2 = 0.05$) due to the elevated scatter of the data (Figure
868 13a). Similar slopes and intercepts were obtained when separately comparing NO_y
869 measurements in smoke from the wildfires and eastern fires (Figures 9b and S13). The slope
870 of 0.81 during the LA Basin flights, may be caused by the lower precision of ΣNO_y than that
871 of the CL NO_y (Figure 9b).
872
873   3.4.2   Discussion and other NO_y measurement comparisons
874 Overall, the agreement between the total NO_y measured by the CL instrument and the ΣNO_y
875 is within instrument uncertainties. Budget closure implies that the historical definition of NO_y
876 (*i.e.*, NO_x and its oxidation products, excluding reduced nitrogen species such as NH_3 and
877 HCN) is adequate even in extremely reactive conditions that foster rapid changes in NO_y
878 speciation. Reduced nitrogen species such as hydrogen cyanide (HCN) or ammonia (NH_3)
879 represent a large fraction of the total nitrogen emission from biomass burning (Roberts et al.,
880 2020) and have been shown to cause a small interference in CL instruments in dry air (Fahey
881 et al., 1985, 1986). This interference is often neglected because of either the low atmospheric
882 abundance of these species or sampling in humid air where such interference is thought to be
883 negligible. Here, we find no evidence for a potential interference of HCN or NH_3, despite
884 their high abundance (tens of ppbv) in smoke plumes (Figure S16). The NO_y to CO ratio was
885 approximately conserved with smoke age, but showed both increasing and decreasing trends
886 with different fires, likely as a result of variability in the NO_x to CO emission ratio during the
887 course of a day with changing fire conditions. Altogether, our findings show that the NO_y
888 instrument provides an accurate and conservative measurement of total reactive nitrogen
889 species, although further work is needed to empirically characterize pNO_3 sampling through
890 the NO_y inlet.
891 There are a few studies that recently examined the NO_y budget closure from aircraft
892 measurements. Juncosa Calahorrano et al. (2021) presented reactive odd nitrogen partitioning
893 during the Western wildfire Experiment for Cloud chemistry, Aerosol absorption and
894 Nitrogen (WE-CAN) that sampled western American wildfires during the summer 2018. The
895 authors found significant (15–26%) contribution of organic N species other than APNs and
896 alkyl nitrates to ΣNO_y. However, there was no total NO_y measurement during WE-CAN, and
897 the conclusion is based on summed individual reactive nitrogen species. The FIREX-AQ
898 comparison of ΣNO_y to total NO_y finds 2-13% of the total NO_y unaccounted for, smaller than
899 the estimate of a 15-26% contribution from multifunctional organic nitrates from WE-CAN.
900 While the FIREX-AQ NO_y difference suggests a smaller contribution from organic nitrates,
901 the WE-CAN estimate is within the uncertainty of the FIREX-AQ analysis. During the

902 WINTER campaign, budget closure of NO_z (=NO_y – NO_x) was demonstrated to occur within
903 20% for all flights following the comparison of ΣNO_z with total NO_z from three different
904 measurement techniques, including a CL instrument (Sparks et al., 2019). A recent ground-
905 based study in New York State in the US found that the sum of the individual reactive odd
906 nitrogen species accounted for 95% of the total NO_y, well within measurement uncertainties
907 (Ninneman et al., 2021). These recent studies contrast with somewhat older literature that
908 often reported a significant shortfall in the NO_y balance, where measured NO_y was higher
909 than ΣNO_y (Hayden et al., 2003; Horii et al., 2005; Williams et al., 1997; Zhang et al., 2008).
910 This shortfall has often been attributed to unmeasured organic N species and more
911 specifically alkyl nitrates (Day et al., 2003; Horii et al., 2005). During FIREX-AQ, C_1–C_5
912 alkyl nitrates accounted for less than 7% on average of the NO_y budget (Figure 10),
913 consistent with findings from other regions in the US (Benedict et al., 2018; Russo et al.,
914 2010). However, FIREX-AQ did not include a measurement of total alkyl nitrates. A recent
915 analysis of the California Rim Fire during the 2013 NASA Studies of Emissions,
916 Atmospheric Composition, Clouds and Climate Coupling by Regional Surveys ($SEAC^4RS$)
917 mission report that total alkyl nitrates measured by TD-LIF accounted for ~10% of the NO_y
918 budget (Wolfe et al., 2022).
919
920 ### 3.5 <u>CO</u>
921 #### 3.5.1 Campaign-wide comparison
922 The 1Hz data comparison between the ICOS and the TDLAS instruments is shown in Figure
923 14. The overall comparison yielded a slope (± combined instrument uncertainties) of 0.98 ±
924 0.03 (R^2 = 0.99) and an intercept of –1.06 ± 0.01 ppbv (Figure 14a). The regression analysis
925 of smoke plume-integrated CO mixing ratios yields a slope of 0.99 (R^2 = 1) for the whole
926 dataset (Figure 14c). A histogram of the absolute difference between CO measurements
927 ($\Delta CO_{ICOS–TDLAS}$) is shown in Figure 5g. 90% of the values were between –6.05 and 2.35 ppbv,
928 and the whole dataset is normally distributed around the central value of the Gaussian fit of –
929 2.87 ± 0.02 ppbv. This is indicative of an offset between the two CO instruments, with the
930 TDLAS systematically higher than the ICOS instrument. This average 2.87 ppbv offset was
931 consistent throughout the campaign regardless of the type of fires that were sampled.
932 Therefore, it cannot explain the significantly lower agreement of the instruments during the
933 eastern fires compared to the wildfires sampling period (Figures 14b and S12). During the
934 first period, the overall slope was 0.99 and ranged from 0.97 to 1.02 (average of 0.99) for
935 individual flights, well within the combined instrument uncertainties of 3% (Figures 14b and
936 S12). However, all individual flight measurements during the eastern fires sampling period
937 exhibit slopes reduced by about 10% (range = 0.86–0.91 with an average of 0.89) and largely
938 positive intercepts (range 6.75–19.04 with an average of 11.51) (Figure S17). As observed for
939 other species, the second period proved to be a more challenging environment for CO
940 measurements. This may be attributed to a spectral issue with one or the other of these two
941 instruments, although we could not identify the source of the discrepancy. $\Delta CO_{ICOS–TDLAS}$
942 exhibit no significant slope with CO (Figure S6g) and H_2O (Figure 6g) mixing ratios.
943
944 #### 3.5.2 Literature aircraft CO measurement comparisons

Overall, the comparison between the two CO instruments shows an agreement well within stated uncertainties. We find that the agreement between the two CO instruments used during FIREX-AQ is well in line with past intercomparisons. During the GTE-CITE experiment, the comparison of a TDLAS technique with two grab sample/gas chromatograph methods for detection of CO showed agreement across the instruments – within the combined instrument uncertainties and strong correlations ($R^2 = 0.85$–0.98) for CO ranging from 60 to 140 ppbv (Hoell et al., 1987). During the North Atlantic Regional Experiment (NARE 97) CO was measured by TDLAS and vacuum ultra-violet fluorescence with agreement to within 11% and systematic offsets of less than 1ppbv (Holloway et al., 2000). CO was also more recently measured by TDLAS and vacuum ultra-violet fluorescence during the side-by-side comparison of instruments aboard two aircraft during the DC3 experiment. There, CO measurements agreed within 5% during flight periods typically ranging from 20 to 30 minutes (Pollack et al., 2016).

4   Conclusion

In this study, we compare airborne measurements of NO, NO_2, HONO, NO_y and CO conducted during the FIREX-AQ campaign in the summer 2019. This dataset offers the opportunity to assess the accuracy of a large suite of detection techniques in a challenging environment where species mixing ratios increased by tens of ppbv in seconds between background air and fire smoke. For NO, NO_2 (CES and LIF), NO_y and CO, correlations agree better than the combined instrument uncertainties, indicating that the stated individual uncertainties are conservative estimates. For NO_2 (CL) and HONO, the percent difference between measurements is higher than the combined instrument uncertainties, indicating potential interferences or calibration inaccuracies that are not identified at this time. Based on the analysis above, we make the following recommendations, which are specific to the FIREX-AQ campaign.

1) Comparison of NO measurements by LIF and CL showed an overall agreement well within instrument uncertainties. Flight-to-flight agreement was generally more variable during the eastern fires sampling period than during the wildfires sampling period, which was attributed to the heterogeneous nature of smoke plumes combined with the physical separation of inlets. Both measurements are considered reliable for FIREX-AQ, although the LIF instrument has better 1Hz precision (1 pptv) than the CL instrument (6 pptv), and the CL instrument exhibited slower time response.

2) Comparison of NO_2 measurements by LIF and CES showed an overall agreement well within the stated instrument uncertainties. However, NO_2 measured by CL is on average 10% higher than that measured by the other two techniques. The agreement worsens for all instruments when comparing NO_2 measured during the eastern fires sampling period, likely for similar reasons as indicated for the NO measurements.

3) The CES and CIMS HONO measurements were highly correlated in each fire plume transect, but the correlation slope of CES vs. CIMS for all 1 Hz data from the entire campaign was 1.80. The HONO measured by CIMS was on average 74% of that measured by

989 CES during the wildfires sampling period, and on average 40% of CES during the eastern
990 fires sampling period. The higher precision data from the CIMS are most useful for analysis
991 of HONO when mixing ratios are lower. The redundancy of HONO measurements during
992 FIREX-AQ led to the discovery that the CIMS sensitivity to HONO was reduced in a high
993 temperature environment. This intercomparison has initiated further studies of the CIMS
994 sensitivity to HONO and other compounds.
995
996 4) Closure of the NO_y budget between the total NO_y measurement by CL and ΣNO_y was
997 achieved for all flights and correlation slopes were usually much better than the combined
998 instrument uncertainties of 25%. NO_x, HNO_3, HONO, APNs and pNO_3 are the main
999 contributors to the NO_y budget, with the other reactive N species contributing less than 10%
1000 on average. We find that the modeled pNO_3 sampling fraction through the NO_y inlet is highly
1001 dependent on altitude, air speed and pNO_3 mass size distribution, and varied on average
1002 between 0.36 and 0.99 during FIREX-AQ. Therefore, approximately 0–24% on average of
1003 the total measured NO_y by CL may be unaccounted for and possibly explained by other
1004 species such as multifunctional organic nitrates. The reason for the secondary positive mode
1005 of 0.4 ppbv in the $\Delta NO_{yCL-Sum}$ distribution in the eastern fires and LA Basin flights could not
1006 be clearly identified. Potential explanations include the contribution of gas-phase organic
1007 nitrates, not included in the ΣNO_y, and/or a water vapor interference in one or more
1008 instruments. Regardless, we conclude that the total NO_y measurement by CL provides a
1009 robust quantification of the reactive nitrogen species in background air as well as in smoke
1010 plumes, and that the total NO_y measurement is not sensitive to interference from reduced
1011 nitrogen species in fire plumes. Further laboratory and field work will be needed to fully
1012 characterize pNO_3 sampling through the NO_y inlet.
1013
1014 5) Comparison of CO measurements by TDLAS and ICOS showed an agreement well within
1015 the combined instrument uncertainties. An offset of ~2 ppbv between the two instruments
1016 was identified but has little impact on the correlation. There was a clear difference in the
1017 agreement between the wildfires sampling period and the eastern fires sampling period,
1018 where the correlation slopes were about 10% lower.
1019
1020 6) Integrating data across smoke plume transects generally improved the correlation between
1021 independent measurements and may be necessary for fire-science related analyses, especially
1022 for smaller plumes with greater spatial heterogeneity compared to the distance between the
1023 sampling locations on a large aircraft.
1024
1025 **Data availability**
1026 All data used in this manuscript are archived online and available at https://www-
1027 air.larc.nasa.gov/cgi-bin/ArcView/firexaq.
1028
1029 **Author contribution**

1030 I.B. and T.B.R. designed research. All authors performed FIREX-AQ measurements. P.C.-J.,
1031 H. G., and J.L.J performed the flow modelling analysis. All authors analyzed data. I.B., J.P.,
1032 J.A.N., and S.S.B. wrote the original draft and all authors edited and revised the paper.
1033

1049 **References**

1050 *Andreae, M. O. (2019). Emission of trace gases and aerosols from biomass burning – an*
1051 *updated assessment. Atmospheric Chemistry and Physics, 19(13), 8523–8546.*
1052 *https://doi.org/10.5194/acp-19-8523-2019*

1053 *Arévalo-Martínez, D. L., Beyer, M., Krumbholz, M., Piller, I., Kock, A., Steinhoff, T., et al.*
1054 *(2013). A new method for continuous measurements of oceanic and atmospheric N_2O, CO*
1055 *and CO_2: performance of off-axis integrated cavity output spectroscopy (OA-ICOS) coupled*
1056 *to non-dispersive infrared detection (NDIR). Ocean Science, 9(6), 1071–1087.*
1057 *https://doi.org/10.5194/os-9-1071-2013*

1058 *Baer, D. S., Paul, J. B., Gupta, M., & O'Keefe, A. (2002). Sensitive absorption measurements*
1059 *in the near-infrared region using off-axis integrated-cavity-output spectroscopy. Applied*
1060 *Physics B, 75(2), 261–265. https://doi.org/10.1007/s00340-002-0971-z*

1061 *Balch, J. K., Bradley, B. A., Abatzoglou, J. T., Nagy, R. C., Fusco, E. J., & Mahood, A. L.*
1062 *(2017). Human-started wildfires expand the fire niche across the United States. Proceedings*
1063 *of the National Academy of Sciences, 114(11), 2946–2951.*
1064 *https://doi.org/10.1073/pnas.1617394114*

1065 *Benedict, K. B., Prenni, A. J., Sullivan, A. P., Evanoski-Cole, A. R., Fischer, E. V., Callahan,*
1066 *S., et al. (2018). Impact of Front Range sources on reactive nitrogen concentrations and*
1067 *deposition in Rocky Mountain National Park. PeerJ, 6, e4759.*
1068 *https://doi.org/10.7717/peerj.4759*

1069 *Bernard, F., Cazaunau, M., Grosselin, B., Zhou, B., Zheng, J., Liang, P., et al. (2016).*
1070 *Measurements of nitrous acid (HONO) in urban area of Shanghai, China. Environmental*
1071 *Science and Pollution Research, 23(6), 5818–5829. https://doi.org/10.1007/s11356-015-*
1072 *5797-4*

1073 *Bertram, T. H., Thornton, J. A., & Riedel, T. P. (2009). An experimental technique for the*
1074 *direct measurement of N_2O_5 reactivity on ambient particles. Atmospheric Measurement*
1075 *Techniques, 2(1), 231–242. https://doi.org/10.5194/amt-2-231-2009*

1076 *Boggs, P. T., Byrd, R. H., & Schnabel, R. B. (1987). A Stable and Efficient Algorithm for*
1077 *Nonlinear Orthogonal Distance Regression. SIAM Journal on Scientific and Statistical*
1078 *Computing, 8(6), 1052–1078. https://doi.org/10.1137/0908085*

1079 *Bollinger, M. J., Sievers, R. E., Fahey, D. W., & Fehsenfeld, F. C. (1983). Conversion of*
1080 *nitrogen dioxide, nitric acid, and n-propyl nitrate to nitric oxide by a gold-catalyzed*
1081 *reduction with carbon monoxide. Analytical Chemistry, 55(12), 1980–1986.*
1082 *https://doi.org/10.1021/ac00262a034*

1083 *Bourgeois, I., Peischl, J., Neuman, J. A., Brown, S. S., Thompson, C. R., Aikin, K. C., et al.*
1084 *(2021). Large contribution of biomass burning emissions to ozone throughout the global*
1085 *remote troposphere. Proceedings of the National Academy of Sciences, 118(52),*
1086 *e2109628118. https://doi.org/10.1073/pnas.2109628118*

1087 *Bowman, D. M. J. S., Balch, J. K., Artaxo, P., Bond, W. J., Carlson, J. M., Cochrane, M. A.,*
1088 *et al. (2009). Fire in the Earth System. Science, 324(5926), 481–484.*
1089 *https://doi.org/10.1126/science.1163886*

1090 *Brock, C. A., Williamson, C., Kupc, A., Froyd, K. D., Erdesz, F., Wagner, N., et al. (2019).*
1091 *Aerosol size distributions during the Atmospheric Tomography Mission (ATom): methods,*
1092 *uncertainties, and data products. Atmospheric Measurement Techniques, 12(6), 3081–3099.*
1093 *https://doi.org/10.5194/amt-12-3081-2019*

1094 *Browne, E. C., Perring, A. E., Wooldridge, P. J., Apel, E., Hall, S. R., Huey, L. G., et al.*
1095 *(2011). Global and regional effects of the photochemistry of $CH_3O_2NO_2$: evidence from*
1096 *ARCTAS. Atmospheric Chemistry and Physics, 11(9), 4209–4219.*
1097 *https://doi.org/10.5194/acp-11-4209-2011*

1098 *Burke, M., Driscoll, A., Heft-Neal, S., Xue, J., Burney, J., & Wara, M. (2021). The changing*
1099 *risk and burden of wildfire in the United States. Proceedings of the National Academy of*
1100 *Sciences, 118(2). https://doi.org/10.1073/pnas.2011048118*

1101 *Canagaratna, M. R., Jayne, J. T., Jimenez, J. L., Allan, J. D., Alfarra, M. R., Zhang, Q., et al.*
1102 *(2007). Chemical and microphysical characterization of ambient aerosols with the aerodyne*
1103 *aerosol mass spectrometer. Mass Spectrometry Reviews, 26(2), 185–222.*
1104 *https://doi.org/10.1002/mas.20115*

1105 *Cazorla, M., Wolfe, G. M., Bailey, S. A., Swanson, A. K., Arkinson, H. L., & Hanisco, T. F.*
1106 *(2015). A new airborne laser-induced fluorescence instrument for in situ detection of*
1107 *formaldehyde throughout the troposphere and lower stratosphere. Atmospheric Measurement*
1108 *Techniques, 8(2), 541–552. https://doi.org/10.5194/amt-8-541-2015*

1109 *Chen, J., Wenger, J. C., & Venables, D. S. (2011). Near-Ultraviolet Absorption Cross*
1110 *Sections of Nitrophenols and Their Potential Influence on Tropospheric Oxidation Capacity.*
1111 *The Journal of Physical Chemistry A, 115(44), 12235–12242.*
1112 *https://doi.org/10.1021/jp206929r*

1113 *Collier, S., Zhou, S., Onasch, T. B., Jaffe, D. A., Kleinman, L., Sedlacek, A. J., et al. (2016).*
1114 *Regional Influence of Aerosol Emissions from Wildfires Driven by Combustion Efficiency:*
1115 *Insights from the BBOP Campaign. Environmental Science & Technology, 50(16), 8613–*
1116 *8622. https://doi.org/10.1021/acs.est.6b01617*

Crilley, L. R., Kramer, L. J., Ouyang, B., Duan, J., Zhang, W., Tong, S., et al. (2019). Intercomparison of nitrous acid (HONO) measurement techniques in a megacity (Beijing). Atmospheric Measurement Techniques, 12(12), 6449–6463. https://doi.org/10.5194/amt-12-6449-2019

Crounse, J. D., McKinney, K. A., Kwan, A. J., & Wennberg, P. O. (2006). Measurement of Gas-Phase Hydroperoxides by Chemical Ionization Mass Spectrometry. Analytical Chemistry, 78(19), 6726–6732. https://doi.org/10.1021/ac0604235

Crutzen, P. J., & Andreae, M. O. (2016). Biomass Burning in the Tropics: Impact on Atmospheric Chemistry and Biogeochemical Cycles. In P. J. Crutzen & H. G. Brauch (Eds.), Paul J. Crutzen: A Pioneer on Atmospheric Chemistry and Climate Change in the Anthropocene (pp. 165–188). Cham: Springer International Publishing. https://doi.org/10.1007/978-3-319-27460-7_7

Day, D. A., Dillon, M. B., Wooldridge, P. J., Thornton, J. A., Rosen, R. S., Wood, E. C., & Cohen, R. C. (2003). On alkyl nitrates, O3, and the "missing NOy." Journal of Geophysical Research: Atmospheres, 108(D16). https://doi.org/10.1029/2003JD003685

Day, D. A., Campuzano-Jost, P., Nault, B. A., Palm, B. B., Hu, W., Guo, H., et al. (2021). A Systematic Re-evaluation of Methods for Quantification of Bulk Particle-phase Organic Nitrates Using Real-time Aerosol Mass Spectrometry. Atmospheric Measurement Techniques Discussions, 1–35. https://doi.org/10.5194/amt-2021-263

DeCarlo, P. F., Kimmel, J. R., Trimborn, A., Northway, M. J., Jayne, J. T., Aiken, A. C., et al. (2006). Field-Deployable, High-Resolution, Time-of-Flight Aerosol Mass Spectrometer. Analytical Chemistry, 78(24), 8281–8289. https://doi.org/10.1021/ac061249n

Decker, Z. C. J., Robinson, M. A., Barsanti, K. C., Bourgeois, I., Coggon, M. M., DiGangi, J. P., et al. (2021). Nighttime and daytime dark oxidation chemistry in wildfire plumes: an observation and model analysis of FIREX-AQ aircraft data. Atmospheric Chemistry and Physics, 21(21), 16293–16317. https://doi.org/10.5194/acp-21-16293-2021

Dennis, A., Fraser, M., Anderson, S., & Allen, D. (2002). Air pollutant emissions associated with forest, grassland, and agricultural burning in Texas. Atmospheric Environment, 36(23), 3779–3792. https://doi.org/10.1016/S1352-2310(02)00219-4

Dibb, J. E., Talbot, R. W., Seid, G., Jordan, C., Scheuer, E., Atlas, E., et al. (2002). Airborne sampling of aerosol particles: Comparison between surface sampling at Christmas Island and P-3 sampling during PEM-Tropics B. Journal of Geophysical Research: Atmospheres, 107(D2), PEM 2-1-PEM 2-17. https://doi.org/10.1029/2001JD000408

Diskin, G. S., Podolske, J. R., Sachse, G. W., & Slate, T. A. (2002). Open-path airborne tunable diode laser hygrometer. In Diode Lasers and Applications in Atmospheric Sensing (Vol. 4817, pp. 196–204). International Society for Optics and Photonics. https://doi.org/10.1117/12.453736

Eisele, F. L., Mauldin, L., Cantrell, C., Zondlo, M., Apel, E., Fried, A., et al. (2003). Summary of measurement intercomparisons during TRACE-P. Journal of Geophysical Research: Atmospheres, 108(D20). https://doi.org/10.1029/2002JD003167

Fahey, D. W., Eubank, C. S., Hübler, G., & Fehsenfeld, F. C. (1985). Evaluation of a catalytic reduction technique for the measurement of total reactive odd-nitrogen NO y in the atmosphere. Journal of Atmospheric Chemistry, 3(4), 435–468.

Fahey, D. W., Hübler, G., Parrish, D. D., Williams, E. J., Norton, R. B., Ridley, B. A., et al. (1986). Reactive nitrogen species in the troposphere: Measurements of NO, NO2, HNO3,

particulate nitrate, peroxyacetyl nitrate (PAN), O3, and total reactive odd nitrogen (NO y) at Niwot Ridge, Colorado. *Journal of Geophysical Research: Atmospheres*, 91(D9), 9781–9793. https://doi.org/10.1029/JD091iD09p09781

Farmer, D. K., Matsunaga, A., Docherty, K. S., Surratt, J. D., Seinfeld, J. H., Ziemann, P. J., & Jimenez, J. L. (2010). Response of an aerosol mass spectrometer to organonitrates and organosulfates and implications for atmospheric chemistry. *Proceedings of the National Academy of Sciences*, 107(15), 6670–6675. https://doi.org/10.1073/pnas.0912340107

Fiedler, S. E., Hese, A., & Ruth, A. A. (2003). Incoherent broad-band cavity-enhanced absorption spectroscopy. *Chemical Physics Letters*, 371(3), 284–294. https://doi.org/10.1016/S0009-2614(03)00263-X

Fisher, J. A., Jacob, D. J., Travis, K. R., Kim, P. S., Marais, E. A., Chan Miller, C., et al. (2016). Organic nitrate chemistry and its implications for nitrogen budgets in an isoprene- and monoterpene-rich atmosphere: constraints from aircraft (SEAC⁴RS) and ground-based (SOAS) observations in the Southeast US. *Atmospheric Chemistry and Physics*, 16(9), 5969–5991. https://doi.org/10.5194/acp-16-5969-2016

Fontijn, Arthur., Sabadell, A. J., & Ronco, R. J. (1970). Homogeneous chemiluminescent measurement of nitric oxide with ozone. Implications for continuous selective monitoring of gaseous air pollutants. *Analytical Chemistry*, 42(6), 575–579. https://doi.org/10.1021/ac60288a034

Fry, J. L., Draper, D. C., Zarzana, K. J., Campuzano-Jost, P., Day, D. A., Jimenez, J. L., et al. (2013). Observations of gas- and aerosol-phase organic nitrates at BEACHON-RoMBAS 2011. *Atmospheric Chemistry and Physics*, 13(17), 8585–8605. https://doi.org/10.5194/acp-13-8585-2013

Galloway, J. N., Aber, J. D., Erisman, J. W., Seitzinger, S. P., Howarth, R. W., Cowling, E. B., & Cosby, B. J. (2003). The Nitrogen Cascade. *BioScience*, 53(4), 341. https://doi.org/10.1641/0006-3568(2003)053[0341:TNC]2.0.CO;2

Gao, R. S., McLaughlin, R. J., Schein, M. E., Neuman, J. A., Ciciora, S. J., Holecek, J. C., & Fahey, D. W. (1999). Computer-controlled Teflon flow control valve. *Review of Scientific Instruments*, 70(12), 4732–4733. https://doi.org/10.1063/1.1150137

Gregory, G. L., Hoell, J. M., Torres, A. L., Carroll, M. A., Ridley, B. A., Rodgers, M. O., et al. (1990). An intercomparison of airborne nitric oxide measurements: A second opportunity. *Journal of Geophysical Research: Atmospheres*, 95(D7), 10129–10138. https://doi.org/10.1029/JD095iD07p10129

Gregory, G. L., Hoell, J. M., Carroll, M. A., Ridley, B. A., Davis, D. D., Bradshaw, J., et al. (1990). An intercomparison of airborne nitrogen dioxide instruments. *Journal of Geophysical Research: Atmospheres*, 95(D7), 10103–10127. https://doi.org/10.1029/JD095iD07p10103

Guo, H., Campuzano-Jost, P., Pagonis, D., Schueneman, M., Day, D. A., Nault, B. A., et al. (2020). Submicron Particle Composition and Acidity in Fire Plumes during FIREX-AQ aircraft study, 2020, A232-10. Presented at the AGU Fall Meeting Abstracts.

Guo, Hongyu, Campuzano-Jost, P., Nault, B. A., Day, D. A., Schroder, J. C., Kim, D., et al. (2021). The importance of size ranges in aerosol instrument intercomparisons: a case study for the Atmospheric Tomography Mission. *Atmospheric Measurement Techniques*, 14(5), 3631–3655. https://doi.org/10.5194/amt-14-3631-2021

1205 *Hall, B. D., Dutton, G. S., & Elkins, J. W. (2007). The NOAA nitrous oxide standard scale for*
1206 *atmospheric observations. Journal of Geophysical Research: Atmospheres, 112(D9).*
1207 *https://doi.org/10.1029/2006JD007954*

1208 *Harder, J. W., & Brault, J. W. (1997). Atmospheric measurements of water vapor in the 442-*
1209 *nm region. Journal of Geophysical Research: Atmospheres, 102(D5), 6245–6252.*
1210 *https://doi.org/10.1029/96JD01730*

1211 *Hayden, K. L., Anlauf, K. G., Hastie, D. R., & Bottenheim, J. W. (2003). Partitioning of*
1212 *reactive atmospheric nitrogen oxides at an elevated site in southern Quebec, Canada.*
1213 *Journal of Geophysical Research: Atmospheres, 108(D19).*
1214 *https://doi.org/10.1029/2002JD003188*

1215 *Hoell, J. M., Gregory, G. L., McDougal, D. S., Sachse, G. W., Hill, G. F., Condon, E. P., &*
1216 *Rasmussen, R. A. (1987). Airborne intercomparison of carbon monoxide measurement*
1217 *techniques. Journal of Geophysical Research: Atmospheres, 92(D2), 2009–2019.*
1218 *https://doi.org/10.1029/JD092iD02p02009*

1219 *Hoell, J. M., Gregory, G. L., McDougal, D. S., Torres, A. L., Davis, D. D., Bradshaw, J., et*
1220 *al. (1987). Airborne intercomparison of nitric oxide measurement techniques. Journal of*
1221 *Geophysical Research: Atmospheres, 92(D2), 1995–2008.*
1222 *https://doi.org/10.1029/JD092iD02p01995*

1223 *Holloway, J. S., Jakoubek, R. O., Parrish, D. D., Gerbig, C., Volz Thomas, A., Schmitgen,*
1224 *S., et al. (2000). Airborne intercomparison of vacuum ultraviolet fluorescence and tunable*
1225 *diode laser absorption measurements of tropospheric carbon monoxide. Journal of*
1226 *Geophysical Research: Atmospheres, 105(D19), 24251–24261.*
1227 *https://doi.org/10.1029/2000JD900237*

1228 *Holmes, C. D., Fite, C., Agastra, A., Schwarz, J. P., Yokelson, R. J., Bui, T. V., & Peterson,*
1229 *D. A. (2020). Critical evaluation of smoke age inferred from different methods during*
1230 *FIREX-AQ, 2020, A225-0010. Presented at the AGU Fall Meeting Abstracts.*

1231 *Jaffe, D. A., O'Neill, S. M., Larkin, N. K., Holder, A. L., Peterson, D. L., Halofsky, J. E., &*
1232 *Rappold, A. G. (2020). Wildfire and prescribed burning impacts on air quality in the United*
1233 *States. Journal of the Air & Waste Management Association, 70(6), 583–615.*
1234 *https://doi.org/10.1080/10962247.2020.1749731*

1235 *Johnston, F. H., Henderson Sarah B., Chen Yang, Randerson James T., Marlier Miriam,*
1236 *DeFries Ruth S., et al. (2012). Estimated Global Mortality Attributable to Smoke from*
1237 *Landscape Fires. Environmental Health Perspectives, 120(5), 695–701.*
1238 *https://doi.org/10.1289/ehp.1104422*

1239 *Johnston, F. H., Borchers-Arriagada, N., Morgan, G. G., Jalaludin, B., Palmer, A. J.,*
1240 *Williamson, G. J., & Bowman, D. M. J. S. (2021). Unprecedented health costs of smoke-*
1241 *related PM2.5 from the 2019–20 Australian megafires. Nature Sustainability, 4(1), 42–47.*
1242 *https://doi.org/10.1038/s41893-020-00610-5*

1243 *Juncosa Calahorrano, J. F., Lindaas, J., O'Dell, K., Palm, B. B., Peng, Q., Flocke, F., et al.*
1244 *(2021). Daytime Oxidized Reactive Nitrogen Partitioning in Western U.S. Wildfire Smoke*
1245 *Plumes. Journal of Geophysical Research: Atmospheres, 126, e2020JD033484.*
1246 *https://doi.org/10.1029/2020JD033484*

1247 *Keller-Rudek, H., Moortgat, G. K., Sander, R., & Sörensen, R. (2013). The MPI-Mainz*
1248 *UV/VIS Spectral Atlas of Gaseous Molecules of Atmospheric Interest. Earth System Science*
1249 *Data, 5(2), 365–373. https://doi.org/10.5194/essd-5-365-2013*

Kenagy, H. S., Sparks, T. L., Ebben, C. J., Wooldrige, P. J., Lopez-Hilfiker, F. D., Lee, B. H., et al. (2018). NOx Lifetime and NOy Partitioning During WINTER. Journal of Geophysical Research: Atmospheres, 123(17), 9813–9827. https://doi.org/10.1029/2018JD028736

Kleffmann, J., Lörzer, J. C., Wiesen, P., Kern, C., Trick, S., Volkamer, R., et al. (2006). Intercomparison of the DOAS and LOPAP techniques for the detection of nitrous acid (HONO). Atmospheric Environment, 40(20), 3640–3652. https://doi.org/10.1016/j.atmosenv.2006.03.027

Kleffmann, Jörg. (2007). Daytime Sources of Nitrous Acid (HONO) in the Atmospheric Boundary Layer. ChemPhysChem, 8(8), 1137–1144. https://doi.org/10.1002/cphc.200700016

Kroll, J. H., & Seinfeld, J. H. (2008). Chemistry of secondary organic aerosol: Formation and evolution of low-volatility organics in the atmosphere. Atmospheric Environment, 42(16), 3593–3624. https://doi.org/10.1016/j.atmosenv.2008.01.003

Lao, M., Crilley, L. R., Salehpoor, L., Furlani, T. C., Bourgeois, I., Neuman, J. A., et al. (2020). A portable, robust, stable, and tunable calibration source for gas-phase nitrous acid (HONO). Atmospheric Measurement Techniques, 13(11), 5873–5890. https://doi.org/10.5194/amt-13-5873-2020

Lareau, N. P., Nauslar, N. J., & Abatzoglou, J. T. (2018). The Carr Fire Vortex: A Case of Pyrotornadogenesis? Geophysical Research Letters, 45(23), 13,107-13,115. https://doi.org/10.1029/2018GL080667

Lee, B. H., Lopez-Hilfiker, F. D., Mohr, C., Kurtén, T., Worsnop, D. R., & Thornton, J. A. (2014). An Iodide-Adduct High-Resolution Time-of-Flight Chemical-Ionization Mass Spectrometer: Application to Atmospheric Inorganic and Organic Compounds. Environmental Science & Technology, 48(11), 6309–6317. https://doi.org/10.1021/es500362a

Lee, Y. R., Ji, Y., Tanner, D. J., & Huey, L. G. (2020). A low-activity ion source for measurement of atmospheric gases by chemical ionization mass spectrometry. Atmospheric Measurement Techniques, 13(5), 2473–2480. https://doi.org/10.5194/amt-13-2473-2020

Lerner, B. M., Gilman, J. B., Aikin, K. C., Atlas, E. L., Goldan, P. D., Graus, M., et al. (2017). An improved, automated whole air sampler and gas chromatography mass spectrometry analysis system for volatile organic compounds in the atmosphere. Atmospheric Measurement Techniques, 10(1), 291–313. https://doi.org/10.5194/amt-10-291-2017

Liousse, C., Guillaume, B., Grégoire, J. M., Mallet, M., Galy, C., Pont, V., et al. (2010). Updated African biomass burning emission inventories in the framework of the AMMA-IDAF program, with an evaluation of combustion aerosols. Atmospheric Chemistry and Physics, 10(19), 9631–9646. https://doi.org/10.5194/acp-10-9631-2010

McCarty, J. L. (2011). Remote Sensing-Based Estimates of Annual and Seasonal Emissions from Crop Residue Burning in the Contiguous United States. Journal of the Air & Waste Management Association, 61(1), 22–34. https://doi.org/10.3155/1047-3289.61.1.22

Meller, R., Raber, W., Crowley, J. N., Jenkin, M. E., & Moortgat, G. K. (1991). The UV-visible absorption spectrum of methylglyoxal. Journal of Photochemistry and Photobiology A: Chemistry, 62(2), 163–171. https://doi.org/10.1016/1010-6030(91)87017-P

Melvin, M. A. (2020). 2020 National Precribed Fire Use Report. National Association of State Foresters. Retrieved from https://www.stateforesters.org/wp-content/uploads/2020/12/2020-Prescribed-Fire-Use-Report.pdf

Min, K.-E., Washenfelder, R. A., Dubé, W. P., Langford, A. O., Edwards, P. M., Zarzana, K. J., et al. (2016). A broadband cavity enhanced absorption spectrometer for aircraft measurements of glyoxal, methylglyoxal, nitrous acid, nitrogen dioxide, and water vapor. Atmospheric Measurement Techniques, 9(2), 423–440. https://doi.org/10.5194/amt-9-423-2016

Miyazaki, Y., Kondo, Y., Takegawa, N., Weber, R. J., Koike, M., Kita, K., et al. (2005). Contribution of particulate nitrate to airborne measurements of total reactive nitrogen. Journal of Geophysical Research: Atmospheres, 110(D15). https://doi.org/10.1029/2004JD005502

Moore, R. H., Wiggins, E. B., Ahern, A. T., Zimmerman, S., Montgomery, L., Campuzano Jost, P., et al. (2021). Sizing response of the Ultra-High Sensitivity Aerosol Spectrometer (UHSAS) and Laser Aerosol Spectrometer (LAS) to changes in submicron aerosol composition and refractive index. Atmospheric Measurement Techniques, 14(6), 4517–4542. https://doi.org/10.5194/amt-14-4517-2021

Murphy, J. G., Thornton, J. A., Wooldridge, P. J., Day, D. A., Rosen, R. S., Cantrell, C., et al. (2004). Measurements of the sum of HO_2NO_2 and $CH_3O_2NO_2$ in the remote troposphere. Atmospheric Chemistry and Physics, 4(2), 377–384. https://doi.org/10.5194/acp-4-377-2004

Nault, B. A., Garland, C., Pusede, S. E., Wooldridge, P. J., Ullmann, K., Hall, S. R., & Cohen, R. C. (2015). Measurements of $CH_3O_2NO_2$ in the upper troposphere. Atmospheric Measurement Techniques, 8(2), 987–997. https://doi.org/10.5194/amt-8-987-2015

Neuman, J. A., Trainer, M., Brown, S. S., Min, K.-E., Nowak, J. B., Parrish, D. D., et al. (2016). HONO emission and production determined from airborne measurements over the Southeast U.S. Journal of Geophysical Research: Atmospheres, 121(15), 2016JD025197. https://doi.org/10.1002/2016JD025197

Ninneman, M., Marto, J., Shaw, S., Edgerton, E., Blanchard, C., & Schwab, J. (2021). Reactive oxidized nitrogen speciation and partitioning in urban and rural New York State. Journal of the Air & Waste Management Association, 71(3), 348–365. https://doi.org/10.1080/10962247.2020.1837289

Novelli, P. C., Elkins, J. W., & Steele, L. P. (1991). The development and evaluation of a gravimetric reference scale for measurements of atmospheric carbon monoxide. Journal of Geophysical Research: Atmospheres, 96(D7), 13109–13121. https://doi.org/10.1029/91JD01108

O'Dell, K., Ford, B., Fischer, E. V., & Pierce, J. R. (2019). Contribution of Wildland-Fire Smoke to US PM2.5 and Its Influence on Recent Trends. Environmental Science & Technology, 53(4), 1797–1804. https://doi.org/10.1021/acs.est.8b05430

Pagonis, D., Campuzano-Jost, P., Guo, H., Day, D. A., Schueneman, M. K., Brown, W. L., et al. (2021). Airborne extractive electrospray mass spectrometry measurements of the chemical composition of organic aerosol. Atmospheric Measurement Techniques, 14(2), 1545–1559. https://doi.org/10.5194/amt-14-1545-2021

Peischl, J., Ryerson, T. B., Holloway, J. S., Parrish, D. D., Trainer, M., Frost, G. J., et al. (2010). A top-down analysis of emissions from selected Texas power plants during TexAQS 2000 and 2006. Journal of Geophysical Research: Atmospheres, 115(D16). https://doi.org/10.1029/2009JD013527

Peng, Q., Palm, B. B., Melander, K. E., Lee, B. H., Hall, S. R., Ullmann, K., et al. (2020). HONO Emissions from Western U.S. Wildfires Provide Dominant Radical Source in Fresh

Wildfire Smoke. Environmental Science & Technology.
https://doi.org/10.1021/acs.est.0c00126

Pinto, J. P., Dibb, J., Lee, B. H., Rappenglück, B., Wood, E. C., Levy, M., et al. (2014).
Intercomparison of field measurements of nitrous acid (HONO) during the SHARP
campaign. Journal of Geophysical Research: Atmospheres, 119(9), 5583–5601.
https://doi.org/10.1002/2013JD020287

Platt, U., Perner, D., Harris, G. W., Winer, A. M., & Pitts, J. N. (1980). Observations of
nitrous acid in an urban atmosphere by differential optical absorption. Nature, 285(5763),
312–314. https://doi.org/10.1038/285312a0

Podolske, J. R., Sachse, G. W., & Diskin, G. S. (2003). Calibration and data retrieval
algorithms for the NASA Langley/Ames Diode Laser Hygrometer for the NASA Transport
and Chemical Evolution Over the Pacific (TRACE-P) mission. Journal of Geophysical
Research: Atmospheres, 108(D20). https://doi.org/10.1029/2002JD003156

Pollack, I. B., Homeyer, C. R., Ryerson, T. B., Aikin, K. C., Peischl, J., Apel, E. C., et al.
(2016). Airborne quantification of upper tropospheric NOx production from lightning in deep
convective storms over the United States Great Plains. Journal of Geophysical Research:
Atmospheres, 121(4), 2002–2028. https://doi.org/10.1002/2015JD023941

Pollack, Ilana B., Lerner, B. M., & Ryerson, T. B. (2010). Evaluation of ultraviolet light-
emitting diodes for detection of atmospheric NO2 by photolysis - chemiluminescence. Journal
of Atmospheric Chemistry, 65(2–3), 111–125. https://doi.org/10.1007/s10874-011-9184-3

Ridley, B. A., & Grahek, F. E. (1990). A Small, Low Flow, High Sensitivity Reaction Vessel
for NO Chemiluminescence Detectors. Journal of Atmospheric and Oceanic Technology,
7(2), 307–311. https://doi.org/10.1175/1520-0426(1990)007<0307:ASLFHS>2.0.CO;2

Ridley, B. A., & Howlett, L. C. (1974). An instrument for nitric oxide measurements in the
stratosphere. Review of Scientific Instruments, 45(6), 742–746.
https://doi.org/10.1063/1.1686726

Ridley, B. A., Grahek, F. E., & Walega, J. G. (1992). A Small High-Sensitivity, Medium-
Response Ozone Detector Suitable for Measurements from Light Aircraft. Journal of
Atmospheric and Oceanic Technology, 9(2), 142–148. https://doi.org/10.1175/1520-
0426(1992)009<0142:ASHSMR>2.0.CO;2

Roberts, J. M., Stockwell, C. E., Yokelson, R. J., de Gouw, J., Liu, Y., Selimovic, V., et al.
(2020). The nitrogen budget of laboratory-simulated western US wildfires during the FIREX
2016 Fire Lab study. Atmospheric Chemistry and Physics, 20(14), 8807–8826.
https://doi.org/10.5194/acp-20-8807-2020

Robinson, M. A., Decker, Z. C. J., Barsanti, K. C., Coggon, M. M., Flocke, F. M., Franchin,
A., et al. (2021). Variability and Time of Day Dependence of Ozone Photochemistry in
Western Wildfire Plumes. Environmental Science & Technology, 55(15), 10280–10290.
https://doi.org/10.1021/acs.est.1c01963

Rollins, A. W., Rickly, P. S., Gao, R.-S., Ryerson, T. B., Brown, S. S., Peischl, J., &
Bourgeois, I. (2020). Single-photon laser-induced fluorescence detection of nitric oxide at
sub-parts-per-trillion mixing ratios. Atmospheric Measurement Techniques, 13(5), 2425–
2439. https://doi.org/10.5194/amt-13-2425-2020

Russo, R. S., Zhou, Y., Haase, K. B., Wingenter, O. W., Frinak, E. K., Mao, H., et al. (2010).
Temporal variability, sources, and sinks of C_1-C_5 alkyl nitrates in coastal New England.

Atmospheric Chemistry and Physics, 10(4), 1865–1883. https://doi.org/10.5194/acp-10-1865-2010

Ryerson, T. B., Huey, L. G., Knapp, K., Neuman, J. A., Parrish, D. D., Sueper, D. T., & Fehsenfeld, F. C. (1999). Design and initial characterization of an inlet for gas-phase NOy measurements from aircraft. Journal of Geophysical Research: Atmospheres, 104(D5), 5483–5492. https://doi.org/10.1029/1998JD100087

Ryerson, T. B., Williams, E. J., & Fehsenfeld, F. C. (2000). An efficient photolysis system for fast-response NO2 measurements. Journal of Geophysical Research: Atmospheres, 105(D21), 26447–26461. https://doi.org/10.1029/2000JD900389

Sachse, G. W., Hill, G. F., Wade, L. O., & Perry, M. G. (1987). Fast-response, high-precision carbon monoxide sensor using a tunable diode laser absorption technique. Journal of Geophysical Research: Atmospheres, 92(D2), 2071–2081. https://doi.org/10.1029/JD092iD02p02071

Selimovic, V., Yokelson, R. J., Warneke, C., Roberts, J. M., de Gouw, J., Reardon, J., & Griffith, D. W. T. (2018). Aerosol optical properties and trace gas emissions by PAX and OP-FTIR for laboratory-simulated western US wildfires during FIREX. Atmospheric Chemistry and Physics, 18(4), 2929–2948. https://doi.org/10.5194/acp-18-2929-2018

Slusher, D. L., Huey, L. G., Tanner, D. J., Flocke, F. M., & Roberts, J. M. (2004). A thermal dissociation–chemical ionization mass spectrometry (TD-CIMS) technique for the simultaneous measurement of peroxyacyl nitrates and dinitrogen pentoxide. Journal of Geophysical Research: Atmospheres, 109(D19). https://doi.org/10.1029/2004JD004670

Sparks, T. L., Ebben, C. J., Wooldridge, P. J., Lopez Hilfiker, F. D., Lee, B. H., Thornton, J. A., et al. (2019). Comparison of Airborne Reactive Nitrogen Measurements During WINTER. Journal of Geophysical Research: Atmospheres, 124(19), 10483–10502. https://doi.org/10.1029/2019JD030700

St. Clair, J. M., Swanson, A. K., Bailey, S. A., & Hanisco, T. F. (2019). CAFE: a new, improved nonresonant laser-induced fluorescence instrument for airborne in situ measurement of formaldehyde. Atmospheric Measurement Techniques, 12(8), 4581–4590. https://doi.org/10.5194/amt-12-4581-2019

Stein, A. F., Draxler, R. R., Rolph, G. D., Stunder, B. J. B., Cohen, M. D., & Ngan, F. (2015). NOAA's HYSPLIT Atmospheric Transport and Dispersion Modeling System. Bulletin of the American Meteorological Society, 96(12), 2059–2077. https://doi.org/10.1175/BAMS-D-14-00110.1

Stockwell, C. E., Yokelson, R. J., Kreidenweis, S. M., Robinson, A. L., DeMott, P. J., Sullivan, R. C., et al. (2014). Trace gas emissions from combustion of peat, crop residue, domestic biofuels, grasses, and other fuels: configuration and Fourier transform infrared (FTIR) component of the fourth Fire Lab at Missoula Experiment (FLAME-4). Atmospheric Chemistry and Physics, 14(18), 9727–9754. https://doi.org/10.5194/acp-14-9727-2014

Stutz, J., Kim, E. S., Platt, U., Bruno, P., Perrino, C., & Febo, A. (2000). UV-visible absorption cross sections of nitrous acid. Journal of Geophysical Research: Atmospheres, 105(D11), 14585–14592. https://doi.org/10.1029/2000JD900003

Theys, N., Volkamer, R., Müller, J.-F., Zarzana, K. J., Kille, N., Clarisse, L., et al. (2020). Global nitrous acid emissions and levels of regional oxidants enhanced by wildfires. Nature Geoscience, 13(10), 681–686. https://doi.org/10.1038/s41561-020-0637-7

Vandaele, A. C., Hermans, C., Simon, P. C., Carleer, M., Colin, R., Fally, S., et al. (1998). Measurements of the NO2 absorption cross-section from 42 000 cm−1 to 10 000 cm−1 (238–1000 nm) at 220 K and 294 K. Journal of Quantitative Spectroscopy and Radiative Transfer, 59(3), 171–184. https://doi.org/10.1016/S0022-4073(97)00168-4

Veres, P. R., Neuman, J. A., Bertram, T. H., Assaf, E., Wolfe, G. M., Williamson, C. J., et al. (2020). Global airborne sampling reveals a previously unobserved dimethyl sulfide oxidation mechanism in the marine atmosphere. Proceedings of the National Academy of Sciences, 117(9), 4505–4510. https://doi.org/10.1073/pnas.1919344117

Volkamer, R., Molina, L. T., Molina, M. J., Shirley, T., & Brune, W. H. (2005). DOAS measurement of glyoxal as an indicator for fast VOC chemistry in urban air. Geophysical Research Letters, 32(8). https://doi.org/10.1029/2005GL022616

Volpe Horii, C., William Munger, J., Wofsy, S. C., Zahniser, M., Nelson, D., & Barry McManus, J. (2005). Atmospheric reactive nitrogen concentration and flux budgets at a Northeastern U.S. forest site. Agricultural and Forest Meteorology, 133(1), 210–225. https://doi.org/10.1016/j.agrformet.2004.08.009

Warneke, C., Trainer, M., Gouw, J. A. de, Parrish, D. D., Fahey, D. W., Ravishankara, A. R., et al. (2016). Instrumentation and measurement strategy for the NOAA SENEX aircraft campaign as part of the Southeast Atmosphere Study 2013. Atmospheric Measurement Techniques, 9(7), 3063–3093. https://doi.org/10.5194/amt-9-3063-2016

Washenfelder, R. A., Langford, A. O., Fuchs, H., & Brown, S. S. (2008). Measurement of glyoxal using an incoherent broadband cavity enhanced absorption spectrometer. Atmospheric Chemistry and Physics, 8(24), 7779–7793. https://doi.org/10.5194/acp-8-7779-2008

von der Weiden, S.-L., Drewnick, F., & Borrmann, S. (2009). Particle Loss Calculator – a new software tool for the assessment of the performance of aerosol inlet systems. Atmospheric Measurement Techniques, 2(2), 479–494. https://doi.org/10.5194/amt-2-479-2009

van der Werf, G. R., Randerson, J. T., Giglio, L., Collatz, G. J., Mu, M., Kasibhatla, P. S., et al. (2010). Global fire emissions and the contribution of deforestation, savanna, forest, agricultural, and peat fires (1997–2009). Atmospheric Chemistry and Physics, 10(23), 11707–11735. https://doi.org/10.5194/acp-10-11707-2010

van der Werf, G. R., Randerson, J. T., Giglio, L., van Leeuwen, T. T., Chen, Y., Rogers, B. M., et al. (2017). Global fire emissions estimates during 1997–2016. Earth System Science Data, 9(2), 697–720. https://doi.org/10.5194/essd-9-697-2017

Warneke, C., Schwarz, J. P., Dibb, J., Kalashnikova, O., Frost, G., Seidel, F., Al-Saadi, J., Brown, S. S., Washenfelder, R., Brewer, A., Moore, R. H., Anderson, B. E., Yacovitch, T., Herndon, S., Liu, S., Jaffe, D., Johnston, N., Selimovic, V., Yokelson, B., Giles, D., Holben, B., Goloub, P., Popovici, I., Trainer, M., Pierce, B., Fahey, D., Roberts, J., Soja, A., Peterson, D., Saide, P. E., Holmes, C., Wang, S., Coggon, M. M., Decker, Z. C. J., Ye, X., Stockwell, C., Xu, L., Gkatzelis, G., Lefer, B., Crawford, J. Fire Influence on Regional to Global Environments and Air Quality (FIREX-AQ). To be submitted. 2022

Westerling, A. L. (2016). Increasing western US forest wildfire activity: sensitivity to changes in the timing of spring. Philosophical Transactions of the Royal Society B: Biological Sciences, 371(1696), 20150178. https://doi.org/10.1098/rstb.2015.0178

Williams, E. J., Roberts, J. M., Baumann, K., Bertman, S. B., Buhr, S., Norton, R. B., & Fehsenfeld, F. C. (1997). Variations in NOy composition at Idaho Hill, Colorado. *Journal of Geophysical Research: Atmospheres, 102(D5),* 6297–6314. https://doi.org/10.1029/96JD03252

Wolfe, G. M., Hanisco, T. F., Arkinson, H. L., Blake, D. R., Wisthaler, A., Mikoviny, T., et al. (2022). Photochemical evolution of the 2013 California Rim Fire: synergistic impacts of reactive hydrocarbons and enhanced oxidants. *Atmospheric Chemistry and Physics, 22(6),* 4253–4275. https://doi.org/10.5194/acp-22-4253-2022

Womack, C. C., Neuman, J. A., Veres, P. R., Eilerman, S. J., Brock, C. A., Decker, Z. C. J., et al. (2017). Evaluation of the accuracy of thermal dissociation CRDS and LIF techniques for atmospheric measurement of reactive nitrogen species. *Atmos. Meas. Tech., 10(5),* 1911–1926. https://doi.org/10.5194/amt-10-1911-2017

Wotawa, G. (2000). The Influence of Canadian Forest Fires on Pollutant Concentrations in the United States. *Science, 288(5464),* 324–328. https://doi.org/10.1126/science.288.5464.324

Xu, L., Crounse, J. D., Vasquez, K., Allen, H. M., Wennberg, P. O., Bourgeois, I., et al. (2021). Ozone chemistry in Western U.S. wildfire plumes. *Science Advances,* in press.

Xu, Z., Liu, Y., Nie, W., Sun, P., Chi, X., & Ding, A. (2019). Evaluating the measurement interference of wet rotating-denuder–ion chromatography in measuring atmospheric HONO in a highly polluted area. *Atmospheric Measurement Techniques, 12(12),* 6737–6748. https://doi.org/10.5194/amt-12-6737-2019

Yokelson, R. J., Griffith, D. W. T., & Ward, D. E. (1996). Open-path Fourier transform infrared studies of large-scale laboratory biomass fires. *Journal of Geophysical Research: Atmospheres, 101(D15),* 21067–21080. https://doi.org/10.1029/96JD01800

Zhang, L., Wiebe, A., Vet, R., Mihele, C., O'Brien, J. M., Iqbal, S., & Liang, Z. (2008). Measurements of reactive oxidized nitrogen at eight Canadian rural sites. *Atmospheric Environment, 42(34),* 8065–8078. https://doi.org/10.1016/j.atmosenv.2008.06.034

Ziemann, P. J., & Atkinson, R. (2012). Kinetics, products, and mechanisms of secondary organic aerosol formation. *Chemical Society Reviews, 41(19),* 6582–6605. https://doi.org/10.1039/C2CS35122F

SPECIES	INSTRUMENT	UNCERTAINTY
NO	CL	$\pm$ (4 % + 6 pptv)
	LIF	$\pm$ (8 % + 1 pptv)
NO$_2$	CL	$\pm$ (7 % + 20 pptv)
	CES	$\pm$ (5% + 0.26 ppbv)
	LIF	$\pm$ (10% + 100 pptv)
HONO	CIMS	$\pm$ (15% + 3 pptv)
	CES	$\pm$ (9% + 0.6 ppbv)
NO$_y$	CL	$\pm$ (12 % + 15 pptv)
	Sum	$\sim$ 25%
CO	TD-LAS	2–7%
	ICOS	$\pm$ (2.0 ppb + 2%)

Table 1 List of measured species and instruments, including the corresponding uncertainties, during FIREX-AQ. For uncertainties given as $\pm$ (x % $\pm$ y pptv), x represents the accuracy, and y represents the 2-sigma precision in 1 s.
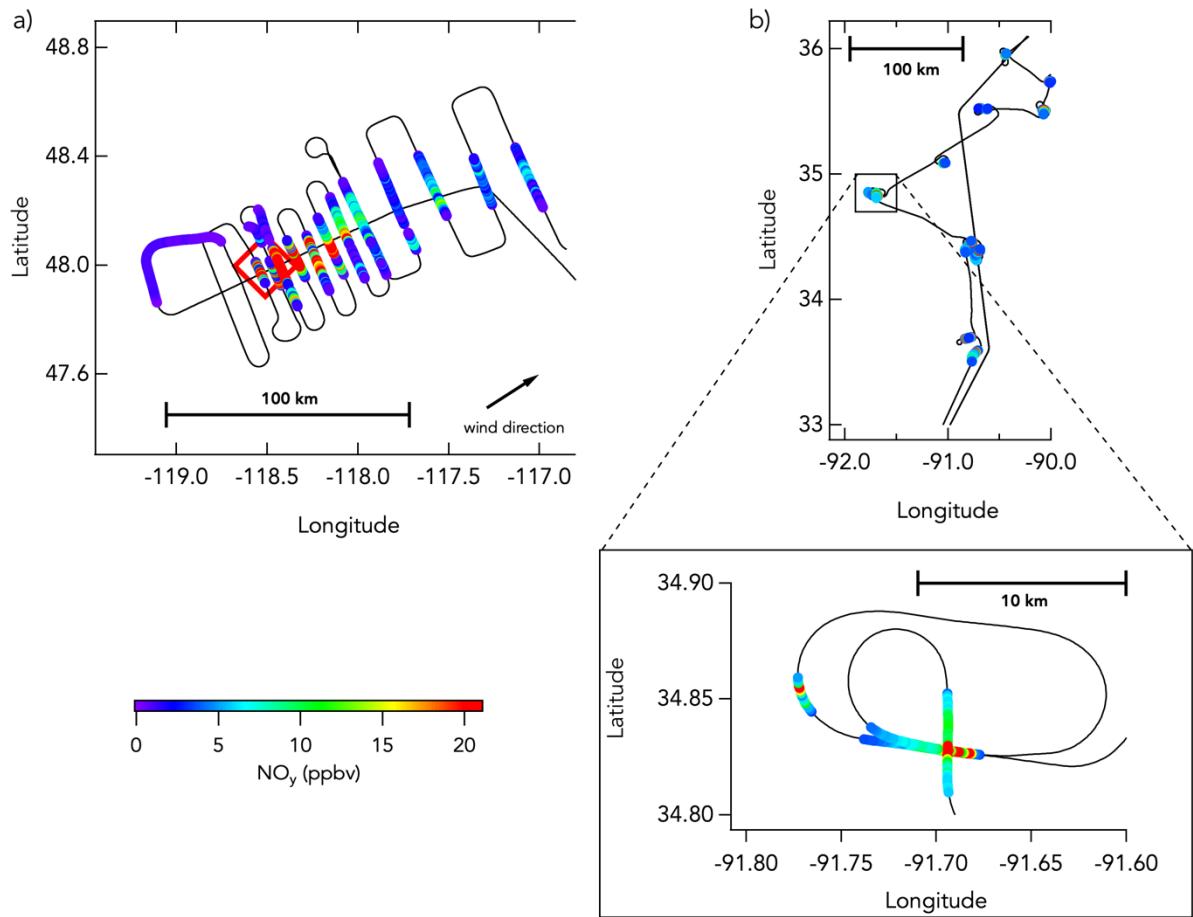
Figure 1 Examples DC-8 flight tracks from western wildfires and eastern agricultural fires. Panel a) shows the DC-8 flight track (black line) during the sampling of the Williams Flat fire (03/08/2019) smoke plume, colored by NO$_y$ mixing ratios (only data in smoke are colored here). Panel b) shows the DC-8 flight track during the sampling of multiple agricultural burns (21/08/2019), also colored by NO$_y$ mixing ratios (only data in smoke are colored here).
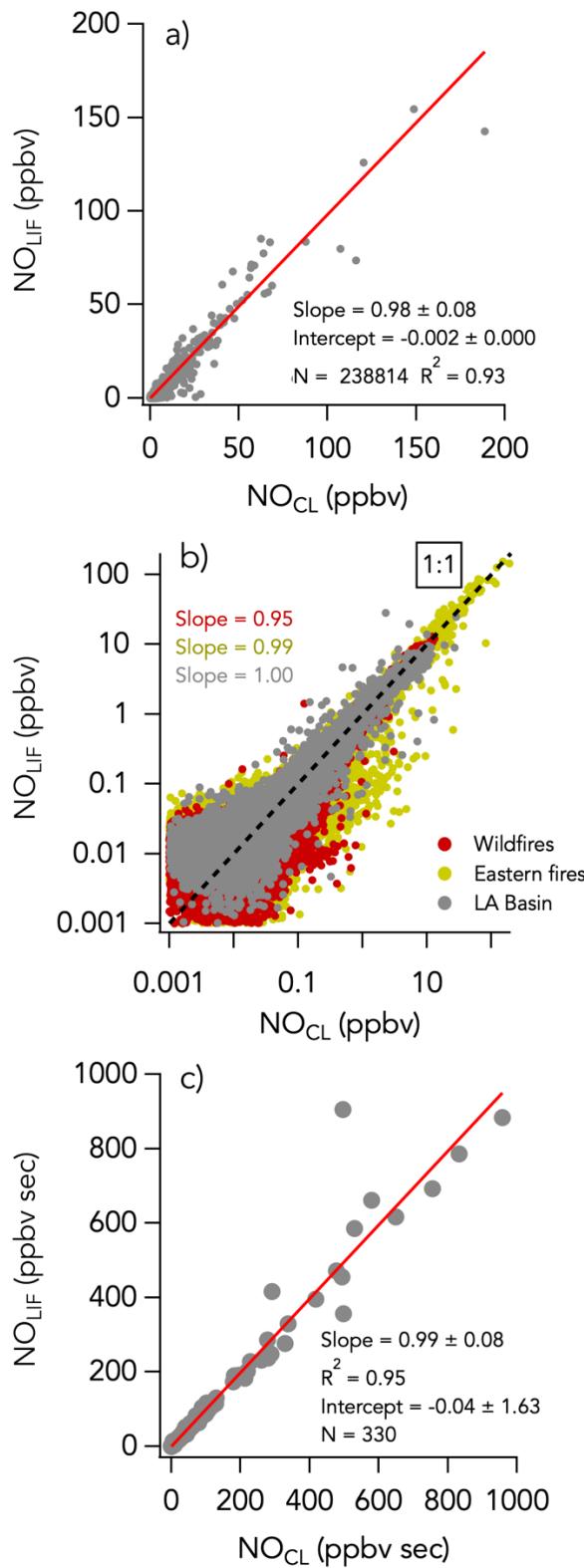
Figure 2 NO measurements by LIF versus CL with a) all 1 s data on a linear scale, b) all 1 s data on a log scale, and c) integrals of 330 crosswind smoke plume transects. N is the number of independent 1 s observations or smoke plume transects that are compared. In panel b, the three sampling periods are shown in different colors with the wildfires sampling period in red, the eastern fires sampling period in mustard, and the Los Angeles (LA) Basin flights in grey. The red lines indicate the fit of the data. The dotted black line is the 1:1 line.
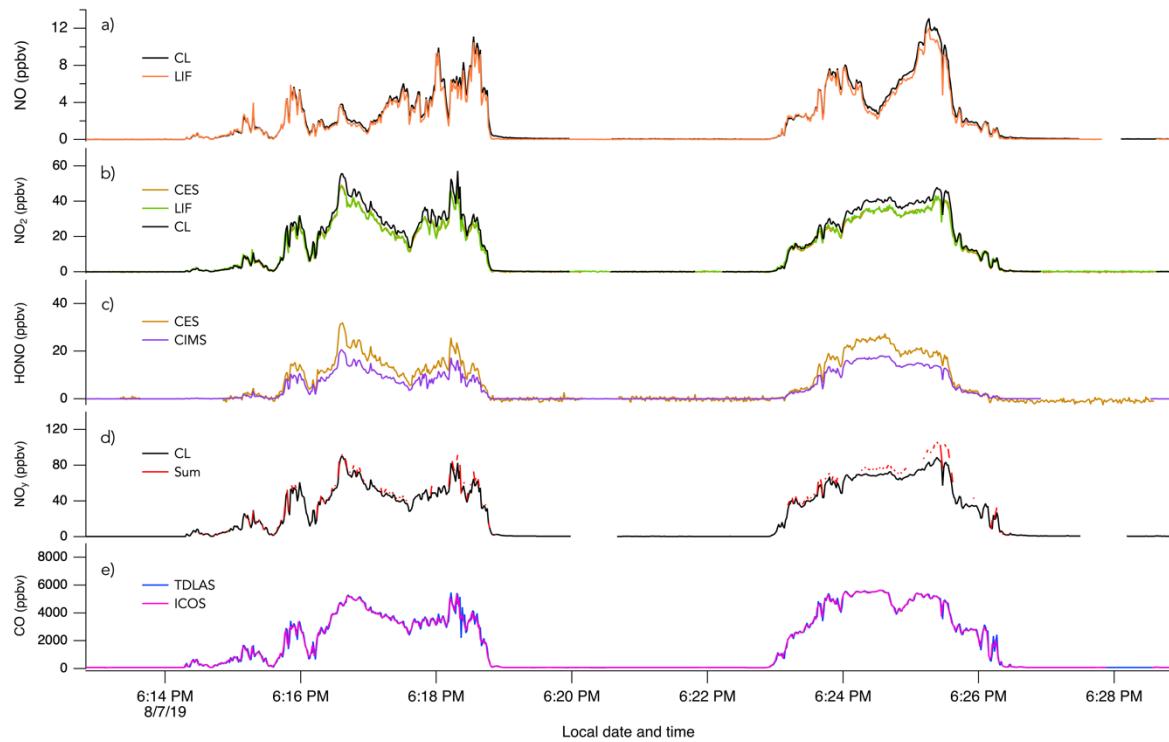
Figure 3 1 s measurements of a) NO, b) NO_2, c) HONO, d) NO_y, and e) CO during two crosswind plume transects of smoke from the Williams Flat fire on 07/08/2019. The plume transects were chosen due to the significant enhancement of all species at that time. Note that in panel b) the NO_2 trace from the CES instrument is hidden behind the NO_2 trace from the LIF instrument.

40
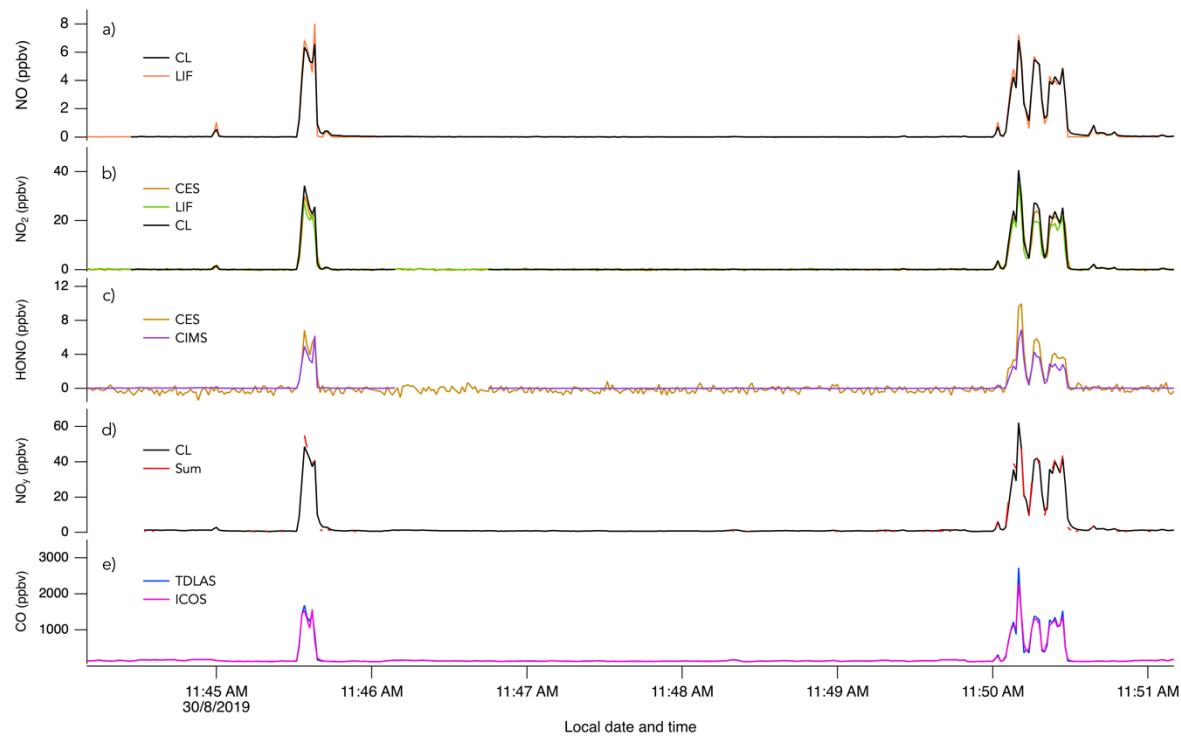
Figure 4 1 s measurements of a) NO, b) NO_2, c) HONO, d) NO_y, and e) CO during crosswind plume transects of smoke from crop burning in southeastern US on 30/08/2019.
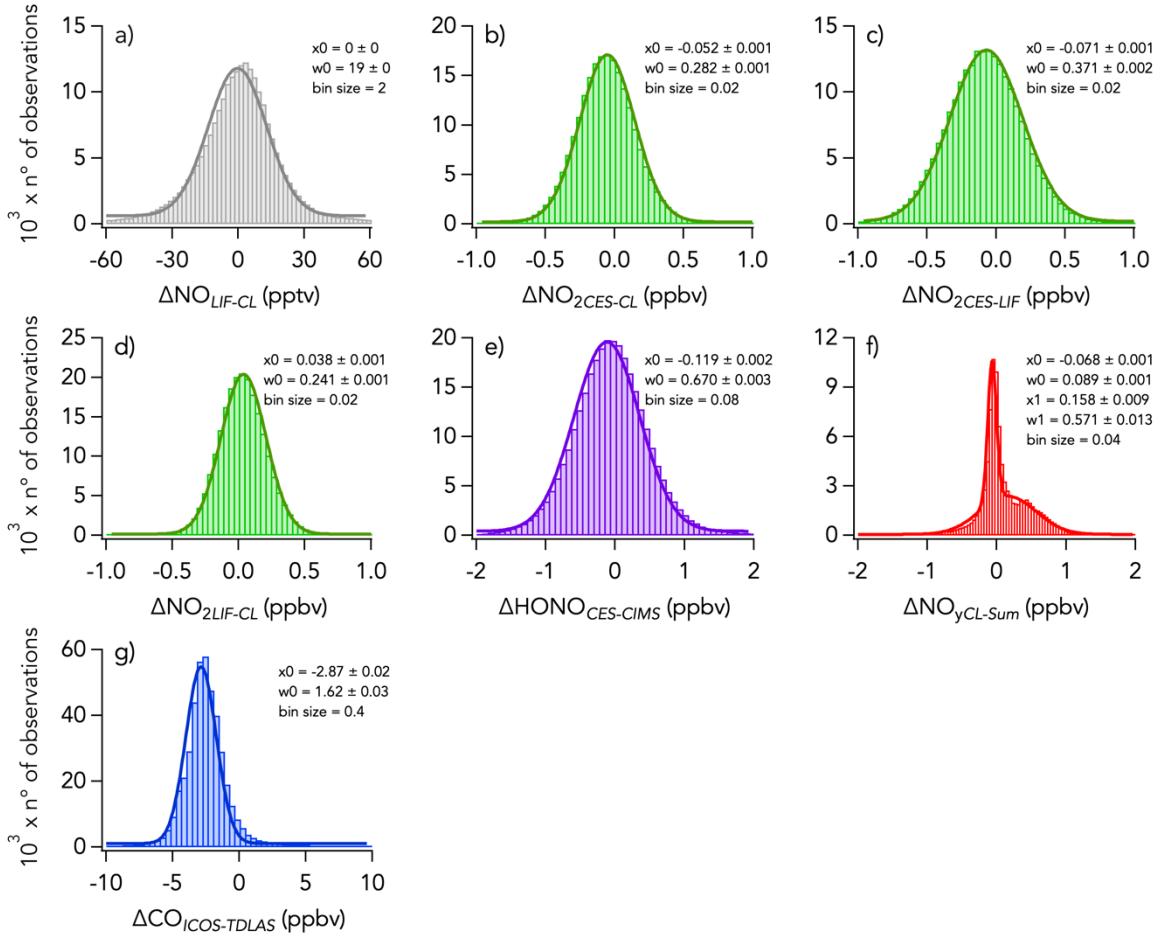
Figure 5 Histograms of the absolute difference of 1 s measurements of a) NO, b)–d) NO_2, e) HONO, f) NO_y, g) CO for the entire campaign. Parameters of the gaussian fit to the histogram is indicated in each panel with x0 and w0 being the central value and the width of the fit, respectively. Note that in panel f) a double gaussian was fitted to the histogram and that the parameters for the second mode are given by x1 and w1.
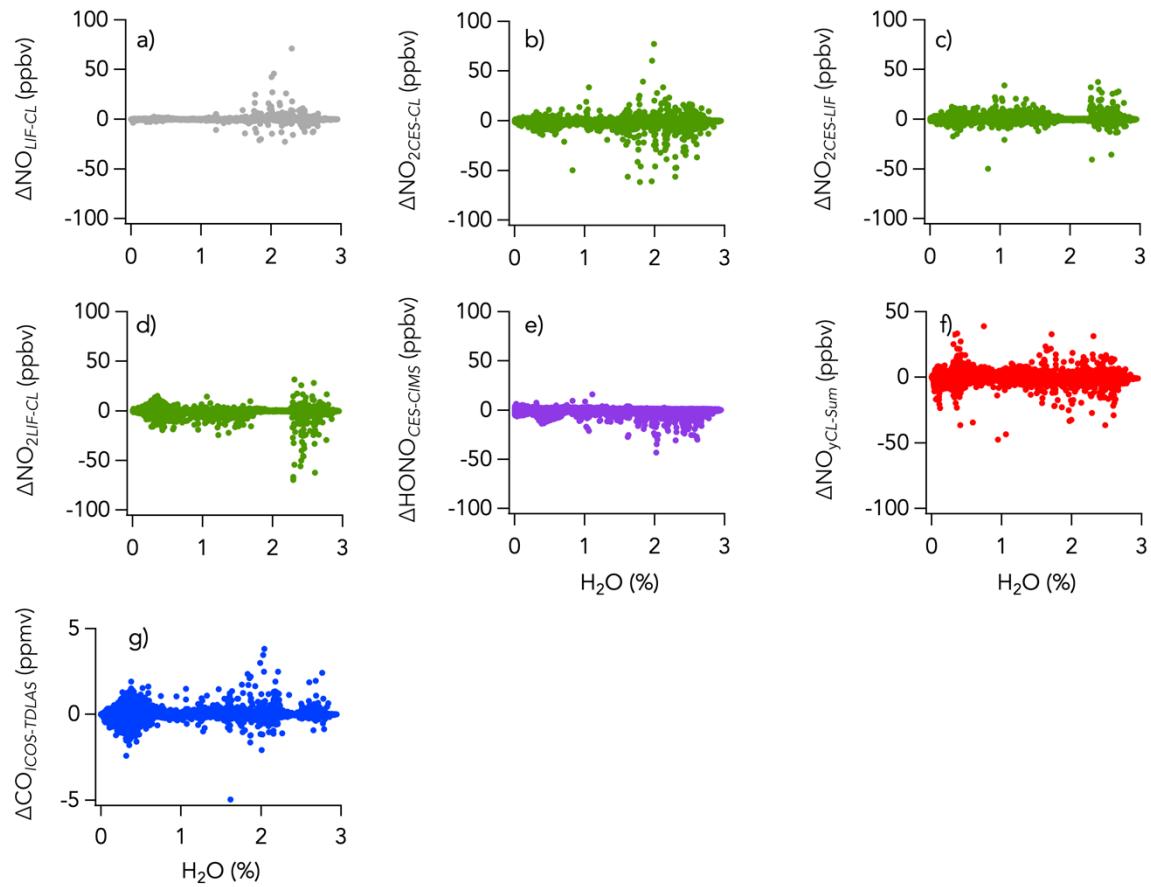
Figure 6 Measurement difference (1 s data) of a) NO, b)–d) NO_2, e) HONO, f) NO_y, g) CO as a function of water vapor for the entire campaign.
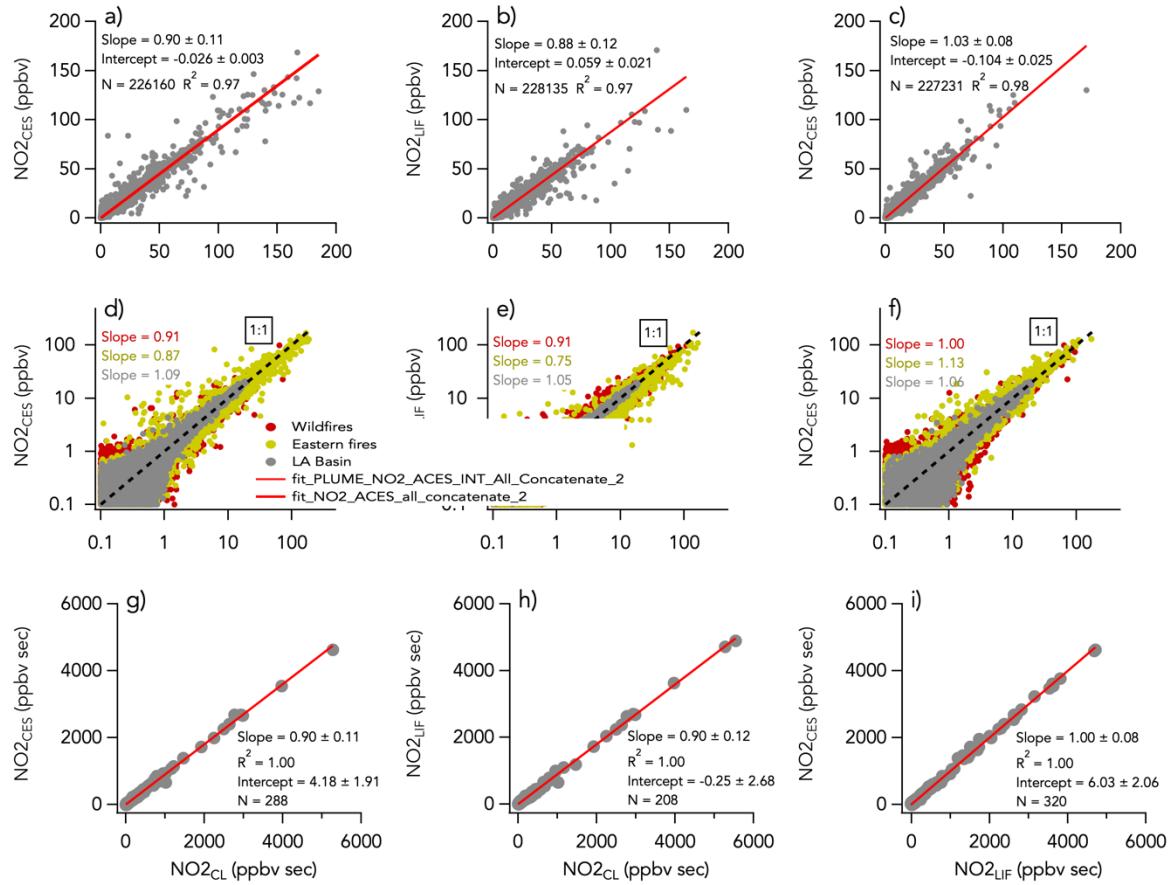
Figure 7 NO$_2$ measurements by LIF, CES and CL with a)–c) all 1 s data on a linear scale, d)–f) all 1 s data on a log scale, and g)–i) integrals of 208–320 crosswind smoke plume transects. N is the number of independent 1 s observations or smoke plume transects that are compared. In the panels d)–f), the three sampling periods are shown in different colors with the wildfires sampling period in red, the eastern fires sampling period in mustard, and the Los Angeles (LA) Basin flights in grey. The red lines indicate the fit of the data. The dotted black lines are the 1:1 line.
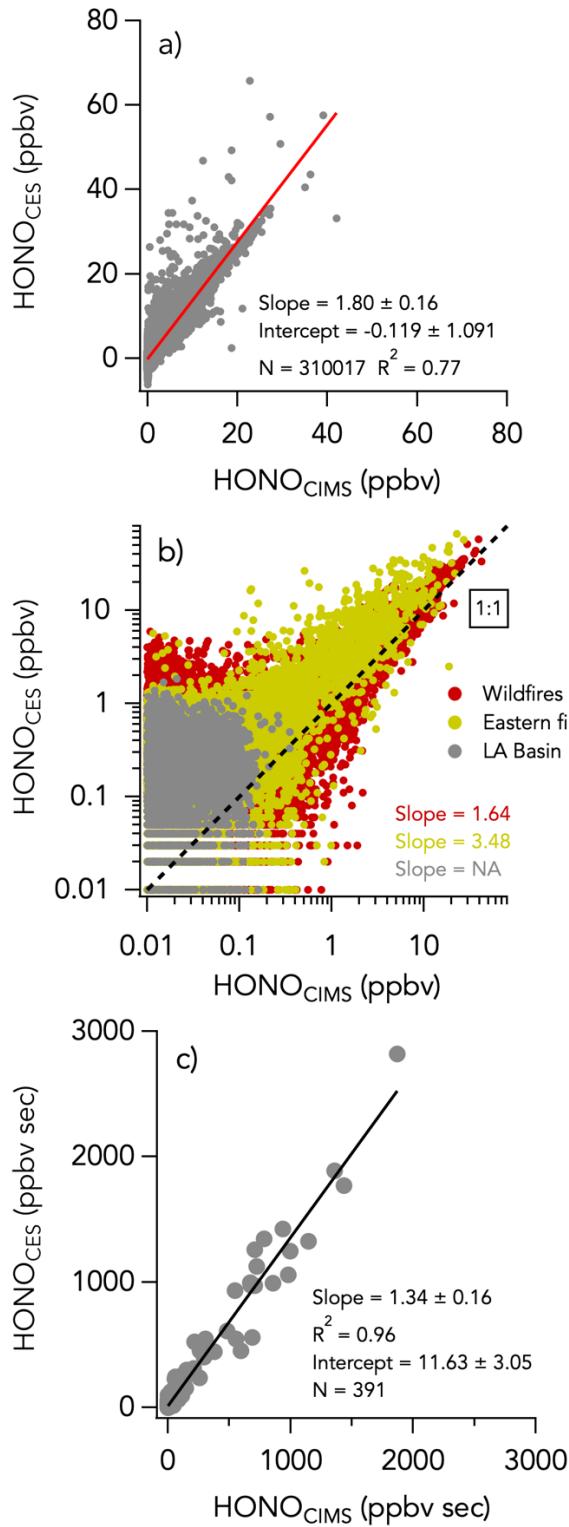
Figure 8 Same as Figure 2 but comparing HONO measurements by CES and CIMS. No slope is given for the Los Angeles (LA) flights in panel as most of the HONO signal at that time was below the instruments' detection limits. Data from the entire campaign are presented in panels a) and b).
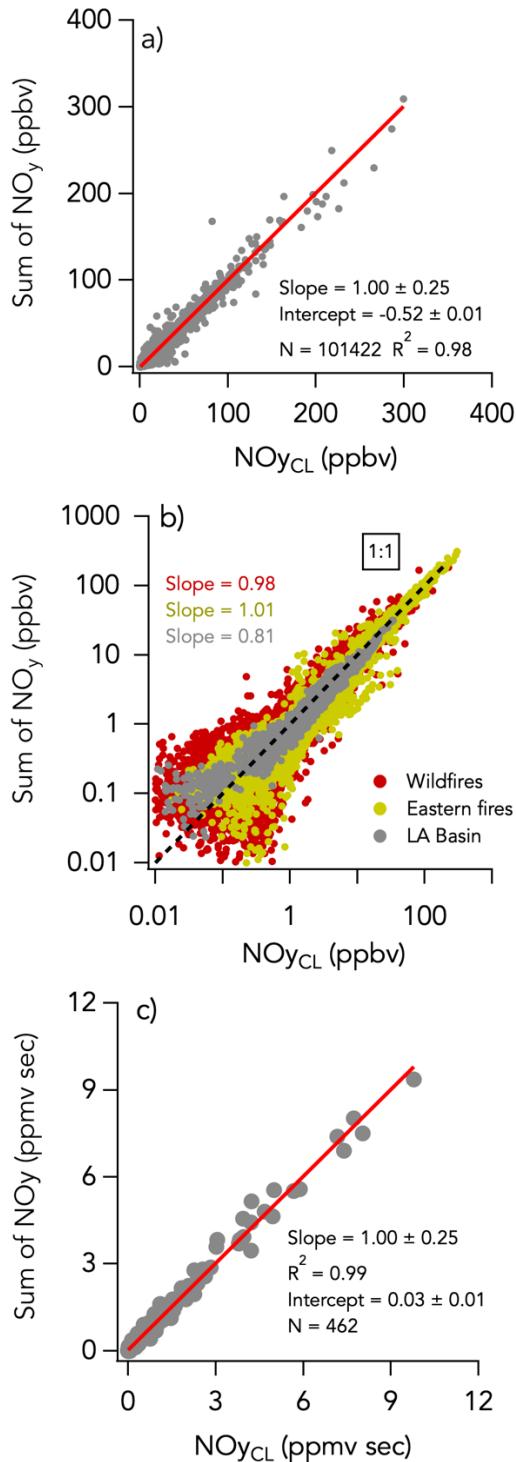
Figure 9 Same as Figure 2 but comparing the sum of individually measured NO_y species (= NO_x + HONO + HNO_3 + APNs + pNO_3) with the total NO_y measurement by CL. Data from the entire campaign are presented in panels a) and b).
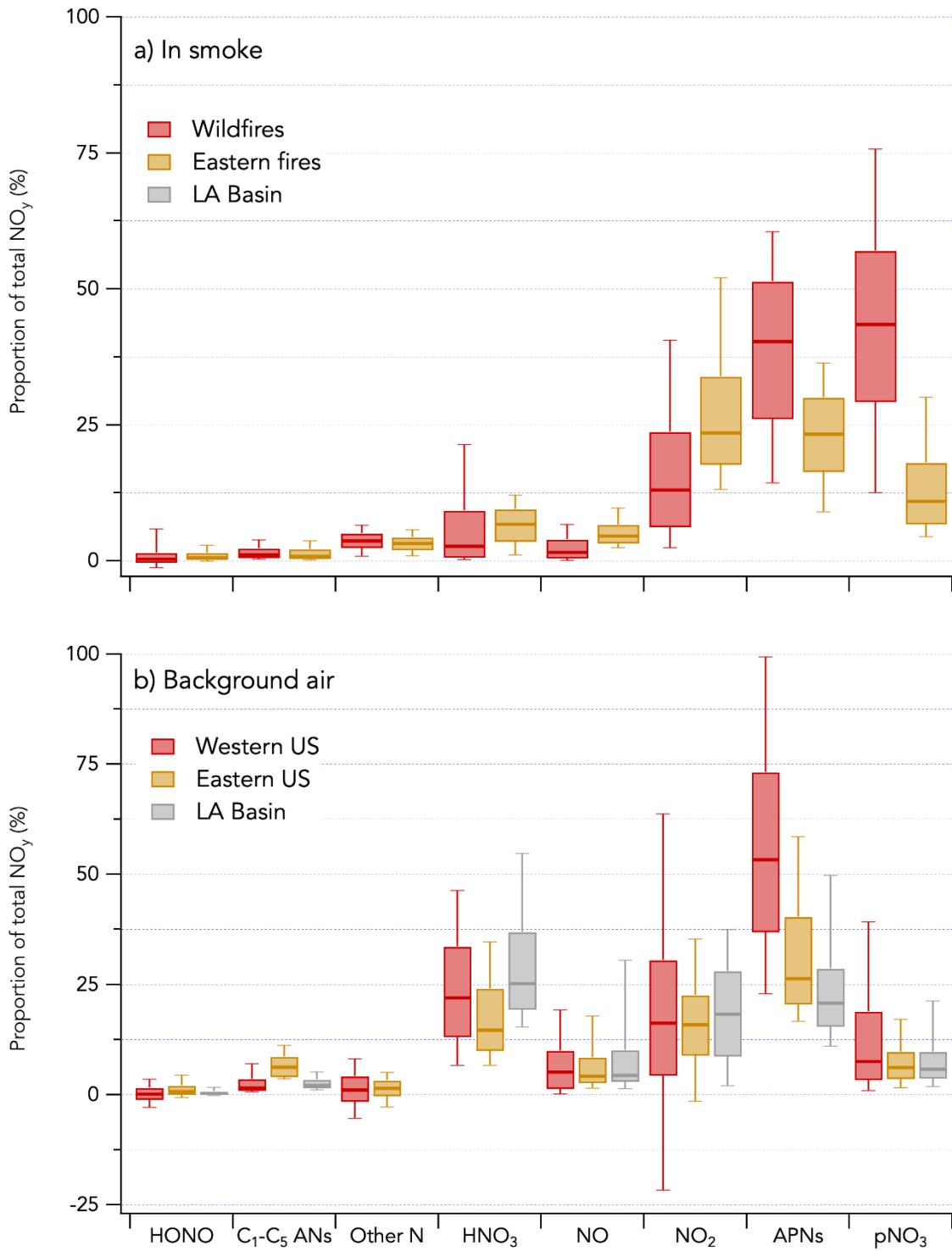
Figure 10 Contribution of individually measured reactive odd nitrogen species to the total NO_y budget during FIREX-AQ. The campaign is separated in three periods (wildfires sampling period in red, eastern fires sampling period in yellow, and Los Angeles (LA) Basin flights in grey). The panel a) show the NO_y budget in smoke plumes, while the panel b) shows that in background air. C_1–C_5 alkyl nitrates are referred to as C_1–C_5 ANs. Other nitrogen species include N_2O_5, CH_3NO_2, and alkene hydroxy nitrates. The box and whisker plots show the 10th, 25th, 50th, 75th, and 90th percentiles.
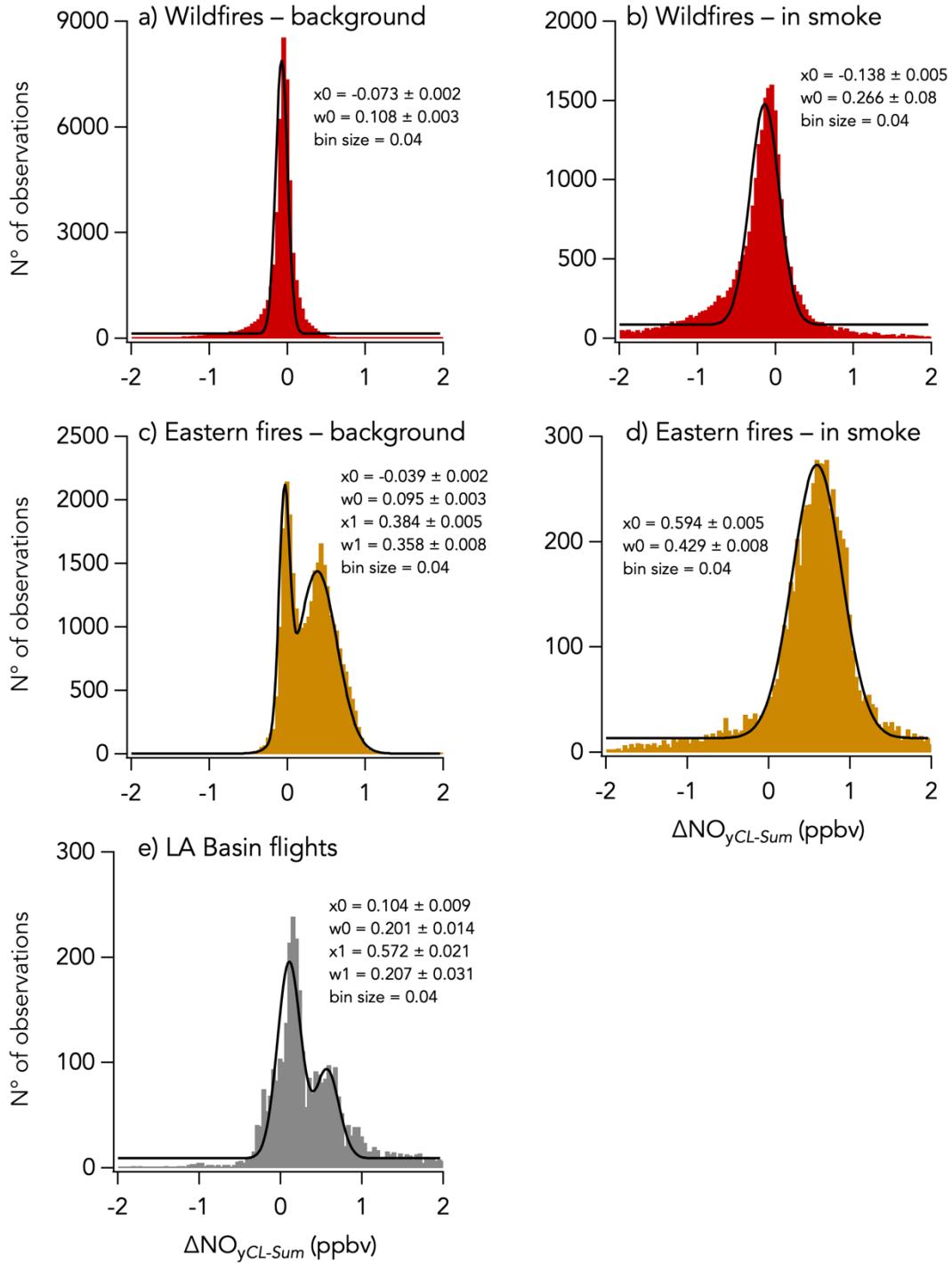
Figure 11 Histograms of $\Delta NO_{yCL\text{-}Sum}$ for three sampling periods during FIREX-AQ with the wildfires sampling period in red, the eastern fires sampling period in yellow, and the Los Angeles (LA) Basin flights in grey. Further separation was made between in smoke measurements (panels b and d) and background air measurements (panels a, c, and e). Parameters of the gaussian fit to the histogram is indicated in each panel with x0 and w0 being the central value and the width of the fit, respectively. Note that in the panels c) and e) a double gaussian was fitted to the histogram and that the parameters for the second mode are given by x1 and w1.
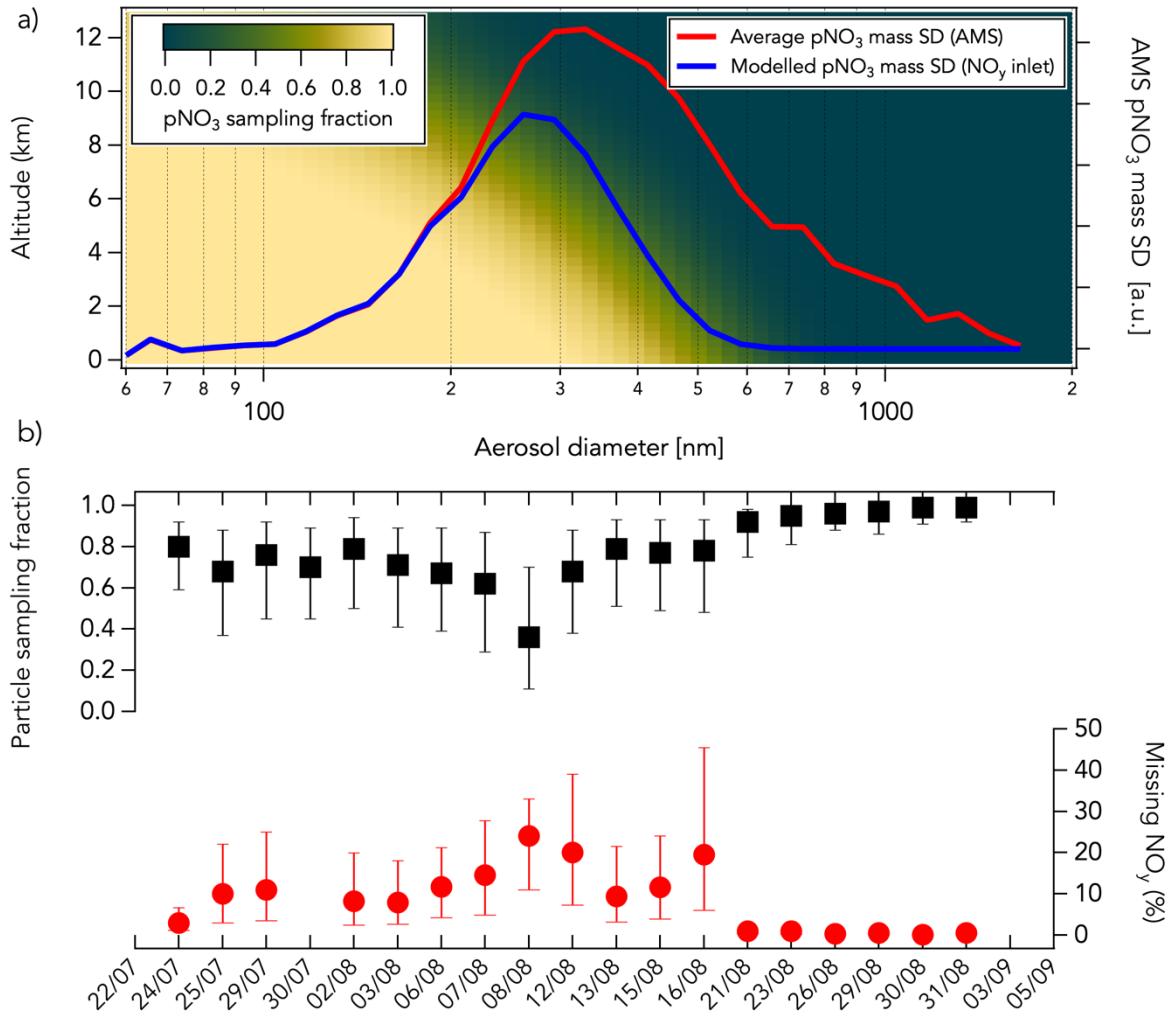
Figure 12 Panel a): The modeled pNO$_3$ sampling fraction through the NO$_y$ inlet as a function of altitude and pNO$_3$ mass size distribution (SD) is shown with a gradient of color from green (low sampling fraction) to yellow (high sampling fraction). The average pNO$_3$ mass size distribution measured in the Williams Flat fire smoke on 07/08/2019 by HR-AMS is shown in red. The modeled pNO$_3$ size distribution sampled in the NO$_y$ inlet assuming an altitude of 5km and a sampled air speed 65% that of the aircraft is shown in blue. In this example case, the sampled pNO$_3$ mass fraction is ~50%. Panel b): The average modeled particle sampling fraction in the NO$_y$ inlet (in black) and the corresponding percentage of measured NO$_y$ that may be unaccounted for (in red) are shown for each flight assuming a sampled air speed of 40% (bottom bars), 65% (markers) and 100% (top bars) that of the aircraft speed. The sampling fractions were calculated using bulk aerosol volume distributions measured by a Laser Aerosol Spectrometer (see Section S1 and Figure SC). The missing NO$_y$ corresponds here to the percentage of measured NO$_y$ that pNO$_3$ not sampled through the NO$_y$ inlet represents. Data shown in the panel b) are from air in smoke only.
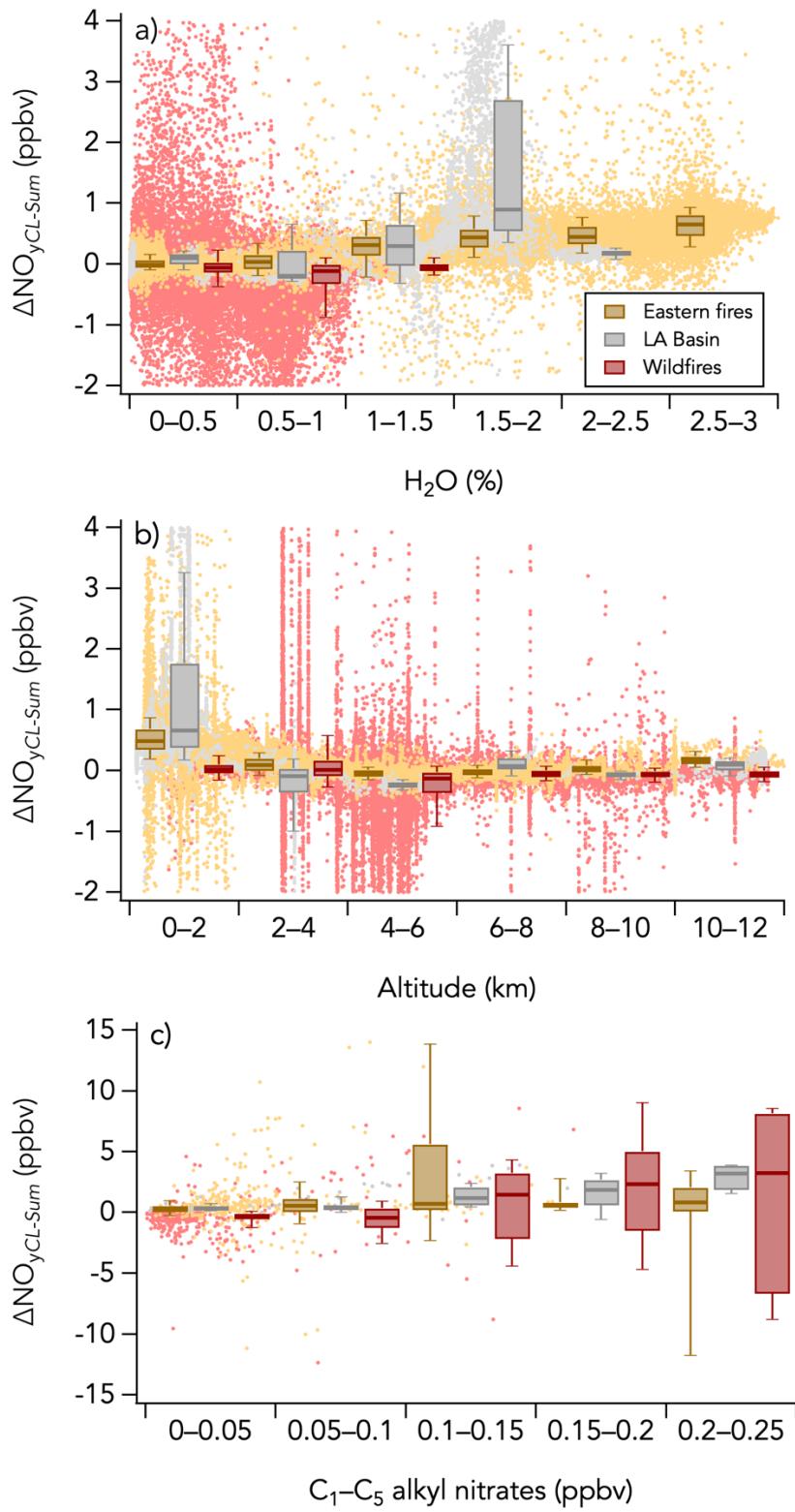
Figure 13 Scatterplots of a) $\Delta NO_{yCL\text{-}Sum}$ vs H_2O, b) $\Delta NO_{yCL\text{-}Sum}$ vs altitude and c) $\Delta NO_{yCL\text{-}Sum}$ vs C_1–C_5 alkyl nitrates measured by the iWAS instrument for three sampling periods during FIREX-AQ (wildfires sampling period in red, eastern fires sampling period in yellow, and Los Angeles (LA) Basin flights in grey). The box and whisker plots show the 10th, 25th, 50th, 75th, and 90th percentiles of $\Delta NO_{yCL\text{-}Sum}$ distributions in each bin. The dots are the 1Hz data in panels a) and b), and 1Hz data averaged to match the iWAS sampling time in panel c).
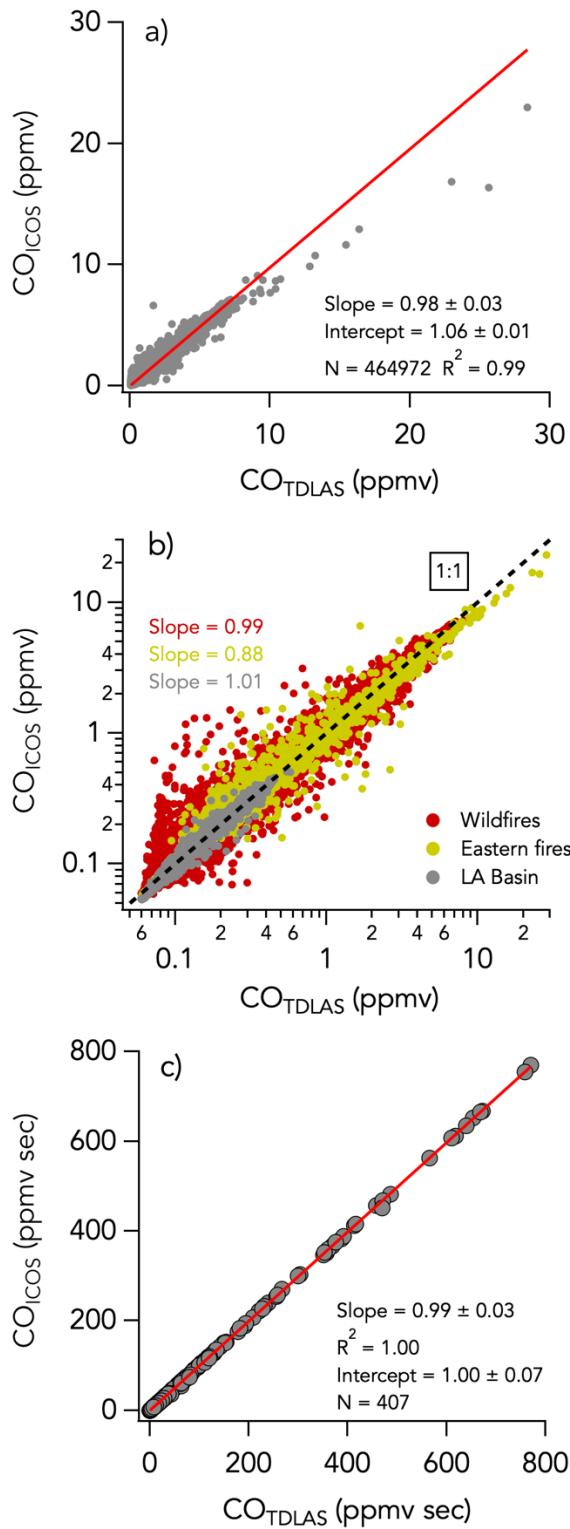
Figure 14 Same as Figure 2 but comparing CO measurements by TDLAS and ICOS.